Probing Z/W pole physics at high-energy muon colliders via vector-boson-fusion processes*

Hao-Qiao Li (李昊桥)[1†] Hai-Ning Yan (严海宁)[1‡] Jiayin Gu (顾嘉荫)[1,2§] Xiao-Ze Tan (谭啸泽)[1,3¶]

[1]Department of Physics and Center for Field Theory and Particle Physics, Fudan University, Shanghai 200438, China
[2]Key Laboratory of Nuclear Physics and Ion-beam Application (MOE), Fudan University, Shanghai 200433, China
[3]Deutsches Elektronen-Synchrotron DESY, Notkestr. 85, 22607 Hamburg, Germany

Abstract: A future e^+e^- collider could run at the Z-pole to perform important electroweak (EW) precision measurements, but such a run may not be viable for a future muon collider. However, this can be compensated for by measuring other EW processes utilizing the high energy and large luminosity of the muon collider. In this paper, we consider the measurements of the vector boson fusion processes of $WW/WZ/W\gamma$ to a pair of fermions (along with a $\nu_\mu\bar{\nu}_\mu$ or $\nu_\mu\mu^+/\bar{\nu}_\mu\mu^-$ pair) at a high-energy muon collider and study their potential for probing EW observables. We consider two run scenarios for the muon collider with center-of-mass energies of 10 and 30 TeV, respectively, and focus on the processes involving $f=b,c,\tau$ and the dimension-6 operators that directly modify the corresponding fermions coupling to the Z/W bosons. The invariant mass distribution of the $f\bar{f}$ pair helps to separate the events from the Z/W and high-energy resonances, whereas the polar angle of the outing fermion provides additional information. Through a chi-squared analysis on the binned distributions and combining the information from the WW and $WZ/W\gamma$ fusion processes, all relevant Wilson coefficients can be constrained simultaneously. The precision surpasses the current EW measurement constraints and is even competitive with future e^+e^- colliders. Our analysis can be included in a more complete framework that is required to fully determine the potential of muon colliders in EW precision measurements.

Keywords: EW measurement, vector boson fusion, SMEFT, muon collider

DOI: 10.1088/1674-1137/addfcd **CSTR:** 32044.14.ChinesePhysicsC.49103102

I. INTRODUCTION

A future high-energy muon collider, if constructed, will have significant physics potential and may unveil some of the deepest mysteries in particle physics. Despite significant technical challenges, the concept of a muon collider was proposed in the early days of particle physics and has recently gained strong interest within the global scientific community [1−3]. The Muon Accelerator Program (MAP), initiated in the United States, presented a concrete framework for developing a muon collider, with an envisioned startup timeline around 2045 [4]. Meanwhile, the European Strategy for Particle Physics (ESPPU), updated in 2020, emphasized the importance of a robust R&D program for muon colliders [5]. This initiative led to the establishment of the International Muon Collider Collaboration (IMCC) [6], tasked with delivering a promising Conceptual Design Report (CDR) in time for the next ESPPU update [7]. Additionally, the European Roadmap for Accelerator R&D [8], published in 2021, included the muon collider as a priority based on recommendations from the particle physics community. This roadmap outlined critical requirements for key technologies and conceptual advances, setting benchmarks for technical assessments such as luminosity goals and the management of detector backgrounds [3]. Over the coming decades, studies on muon colliders are expected to play an increasingly pivotal role in particle physics, offer-

Received 1 April 2025; Accepted 3 June 2025; Published online 4 June 2025

* Supported by the National Natural Science Foundation of China (NSFC) (12035008, 12375091, 12347171), and the Innovation Program for Quantum Science and Technology (2024ZD0300101). Xiao-Ze Tan also acknowledges the support from Helmholtz – OCPC (Office of China Postdoctoral Council) Postdoctoral Fellowship Program

† E-mail: hqli22@m.fudan.edu.cn
‡ E-mail: hnyan22@m.fudan.edu.cn
§ E-mail: jiayin_gu@fudan.edu.cn
¶ E-mail: xz_tan@fudan.edu.cn

ing unique opportunities to explore physics at unprecedented energy scales.

The main advantage of a muon collider, compared with an e^+e^- collider (such as the CEPC [9, 10], FCC-ee [11, 12], ILC [13], C^3 [14], and CLIC [15, 16]), is that it can reach a higher center-of-mass (c.o.m.) energy, possibly up to 10 TeV or even 30 TeV [2, 3] owing to the larger muon mass, which significantly reduces the synchrotron radiation effects. A possible 3 TeV run is also under consideration [17], whereas a 125 GeV run as a first stage to produce Higgs boson on *s*-channel resonance could still be strategically advantageous from both physics and accelerator perspectives [18−20]. With the advantage of reaching the highest possible energy and directly searching for new physics beyond the Standard Model (BSM), a muon collider has limitations on the electroweak (EW) precision program owing to the lack of a *Z*-pole run, as opposed to an e^+e^- collider.

However, all is not lost. The lack of a *Z*-pole program can be compensated for by exploiting other EW measurements. This is evident in the framework of the Standard Model Effective Field Theory (SMEFT), where new physics effects are systematically parametrized in terms of a series of higher dimensional operators, and the relationships among different couplings imposed by the SM gauge groups are automatically imposed. Two important aspects should be considered for the EW analysis under the SMEFT framework. The first is that the contributions of a large set of higher dimensional operators have energy enhancements, and measuring the corresponding processes at the highest possible energy is advantageous, despite a possible smaller SM cross section. A typical example is the diboson ($WW/WZ/Vh$) processes, as their measurements at a high energy muon collider can have competitive or even better reaches on certain EW operators compared with the future *Z*-pole program [21, 22]. However, diboson production is not directly sensitive to the fermion couplings other than those of muons, whereas the subsequent decays of W or Z (which do depend on fermion couplings) do not exhibit energy enhancements. The second aspect is that the cross sections of vector boson fusion (VBF) processes increase with the collider energy, and a large number of events can be collected at the high energy runs, effectively turning the high energy into high precision [22−27].

In this study, we further investigate the potential of EW measurements at a high energy muon collider by performing phenomenological analyses of the fusion processes of two vector bosons (with at least one W boson, *i.e.,* $WW/WZ/W\gamma$) into a pair of fermions (along with a $\nu_\mu\bar{\nu}_\mu$ or $\nu_\mu\mu^+/\bar{\nu}_\mu\mu^-$ pair coming from the incoming $\mu^+\mu^-$), which we collectively denote as VBF$\to 2f$ [1]. We focus on cases with bottom, charm, or tau fermions in the final states, and consider the operators that directly modify their couplings to the W/Z bosons. As mentioned earlier, these operators cannot be directly probed by the diboson production processes without additional flavor assumptions; thus, the measurements of the VBF processes provide valuable complementary information. In addition, the invariant mass distribution of the fermion pair contains useful information, which can be extracted with a binned analysis [2]. By combining the measurements of different fusion processes and exploiting the differential information, all relevant operator coefficients can be constrained simultaneously. In some cases, the reaches are even competitive with those of future e^+e^- colliders.

The remainder of this paper is organized as follows: In Section II, we provide an overview of the relevant dimension-6 SMEFT operators and details of the VBF$\to 2f$ processes with a discussion on their characteristic features. Our results are provided in Section IV, which include detailed comparisons that illustrate the importance of the differential information and the complementarity of the WW and $WZ/W\gamma$ fusion processes. The overall reaches of the Wilson coefficients from our analysis are summarized in Fig. 10. Finally, the conclusion is drawn in Section V. The numerical expressions for the binned cross sections are provided in Appendix A for all the processes included in our analysis. Additional results are provided in Appendix B.

II. THEORETICAL FRAMEWORK

A. Dimension-6 operators in SMEFT

The SMEFT Lagrangian can be obtained by adding a series of higher dimensional operators, characterized by the energy scale Λ, to the SM Lagrangian [28, 29]. Assuming baryon and lepton numbers are conserved around the TeV scale, all higher dimensional operators are of even dimensions,

$$\mathcal{L}_{\rm SMEFT} = \mathcal{L}_{\rm SM} + \sum_i \frac{c_i^{(6)}}{\Lambda^2} O_i^{(6)} + \sum_j \frac{c_j^{(8)}}{\Lambda^4} O_j^{(8)} + \cdots \qquad (1)$$

where the leading new physics contributions are given by the dimension-6 operators. The phenomenology of the SMEFT dimension-6 operators is an active field, with many global analyses already performed for EW, Higgs, and top measurements at both current and future col-

1) The VBF$\to 2f$ processes considered here do not necessarily involve an *s*-channel W/Z boson, in which case the use of the term "fusion" is somewhat inaccurate. For convenience, we simply use the term "VBF$\to 2f$" throughout this paper to denote the two-vector-boson-to-two-fermion processes, with at least one of the two vector bosons being W. We also decided to avoid using the term "vector boson scattering" (VBS) which is often reserved for $VV\to VV$ processes.

2) For the $WZ/W\gamma$ fusion processes with lepton final states, the invariant mass can not be reconstructed due to the missing neutrino.

liders [30−61]. A similar global analysis that includes all the EW measurements at a muon collider should also be performed to fully understand the physics potential. However, such an analysis is beyond the scope of our current study. Instead, we focus on the set of operators that directly modifies the couplings of fermions to the gauge bosons (*Vff*-type couplings), which are

$$\begin{aligned} O_{Hl}^{(1)} &= (H^\dagger i\overleftrightarrow{D}_\mu H)(\bar{\ell}\gamma^\mu \ell), \\ O_{Hl}^{(3)} &= (H^\dagger i\overleftrightarrow{D}^i_\mu H)(\bar{\ell}\sigma^i\gamma^\mu \ell), \\ O_{He} &= (H^\dagger i\overleftrightarrow{D}_\mu H)(\bar{e}\gamma^\mu e), \end{aligned} \tag{2}$$

and similar ones for the quarks,

$$\begin{aligned} O_{Hq}^{(3)} &= (H^\dagger i\overleftrightarrow{D}^i_\mu H)(\bar{q}\sigma^i\gamma^\mu q), \\ O_{Hu} &= (H^\dagger i\overleftrightarrow{D}_\mu H)(\bar{u}\gamma^\mu u), \\ O_{Hd} &= (H^\dagger i\overleftrightarrow{D}_\mu H)(\bar{d}\gamma^\mu d), \end{aligned} \tag{3}$$

where

$$H^\dagger i\overleftrightarrow{D}_\mu H = H^\dagger(iD_\mu H) - (iD_\mu H^\dagger)H, \tag{4}$$

$$H^\dagger i\overleftrightarrow{D}^i_\mu H = H^\dagger\sigma^i(iD_\mu H) - (iD_\mu H^\dagger)\sigma^i H, \tag{5}$$

and the flavor/generation indices are not explicitly written out. After EW symmetry breaking, they generate modifications to the SM *Vff*-type couplings (as well as $hVff$ contact interactions, which we do not consider in this study), which can be parameterized as

$$\begin{aligned} \mathcal{L} \supset\ & -\frac{g}{c_W}Z_\mu\Bigg[\sum_{f=u,d,e,\nu}\bar{f}_L\gamma^\mu(T_f^3 - s_W^2 Q_f + \delta g_L^{Zf})f_L \\ & + \sum_{f=u,d,e}\bar{f}_R\gamma^\mu(-s_W^2 Q_f + \delta g_R^{Zf})f_R\Bigg] \\ & - \frac{g}{\sqrt{2}}\Big[W_\mu^+\bar{u}_L\gamma^\mu(V_{\rm CKM} + \delta g_L^{Wq})d_L \\ & + W_\mu^+\bar{\nu}_L\gamma^\mu(1+\delta g_L^{W\ell})e_L + \text{h.c.}\Big], \end{aligned} \tag{6}$$

where u,d,e collectively denote the corresponding fermions of all three generations. Assuming $V_{\rm CKM} = 1$ for simplicity, the modifications of the *Vff*-type couplings are related to the Wilson coefficients by

$$\begin{aligned} \delta g_L^{Ze} &= -(c_{H\ell}^{(1)} + c_{H\ell}^{(3)})\frac{v^2}{2\Lambda^2}, \quad \delta g_R^{Ze} = -c_{He}\frac{v^2}{2\Lambda^2}, \\ \delta g_L^{Wl} &= c_{Hl}^{(3)}\frac{v^2}{\Lambda^2}, \quad \delta g_L^{Zu} = -(c_{Hq}^{(1)} - c_{Hq}^{(3)})\frac{v^2}{2\Lambda^2}, \\ \delta g_R^{Zu} &= -c_{Hu}\frac{v^2}{2\Lambda^2}, \quad \delta g_L^{Zd} = -(c_{Hq}^{(1)} + c_{Hq}^{(3)})\frac{v^2}{2\Lambda^2}, \\ \delta g_R^{Zd} &= -c_{Hd}\frac{v^2}{2\Lambda^2}, \quad \delta g_L^{Wq} = c_{Hq}^{(3)}\frac{v^2}{\Lambda^2}, \end{aligned} \tag{7}$$

where the generation indices are not explicitly written.

We assume that all operators/couplings are flavor diagonal and focus on those that contribute to the processes involving b, c, or τ (as listed later in Section II.B), whereas the couplings of different generations are allowed to be different (*i.e.,* flavor universality is not imposed). The reasons for our choices are as follows. First, operators that generate universal corrections tend to be better constrained by other measurements, such as the W mass measurement, or the measurement of diboson or Vh processes, which have a considerably larger (effective) c.o.m. energy [22]. Assuming this is the case, setting their effects to zero for the VBF$\to 2f$ processes is a reasonable approximation. The same applies for the EW operators that involve the electron or the muon. For instance, we need not consider the process $W^+W^-\to\mu^+\mu^-$ when the reverse one, $\mu^+\mu^-\to W^+W^-$, is available with a considerably larger c.o.m. energy. Processes involving only the light quarks (u,d,s) are difficult to tag, and the corresponding operators cannot be well constrained without additional flavor assumptions. Finally, the processes involving the top quark are crucial but are left for future studies as the kinematics are much more complicated owing to the top decay.

Throughout most of this paper, we will omit the generation indices of the Wilson coefficients for simplicity, which is hopefully clear from the content. (Note again that we do not assume flavor universality in our study.) For the bounds summarized in Fig. 10, the generations are denoted by subscripts $1,2,3$.

B. Processes

We consider the vector boson fusion processes that produce a pair of fermions (VBF$\to 2f$) where at least one of the fermions is b, c, or τ. More explicitly, including all final state particles, we consider the following five $\mu^-\mu^+\to 4f$ processes:

$$\begin{aligned} &\mu^-\mu^+\to b\bar{b}\nu_\mu\bar{\nu}_\mu, \quad \mu^-\mu^+\to c\bar{c}\nu_\mu\bar{\nu}_\mu, \quad \mu^-\mu^+\to\tau^-\tau^+\nu_\mu\bar{\nu}_\mu, \\ &\mu^-\mu^+\to cs\nu_\mu\mu, \quad \mu^-\mu^+\to\tau\nu_\tau\nu_\mu\mu, \end{aligned} \tag{8}$$

where, by $cs\nu_\mu\mu$, we denote the combination of $c\bar{s}\bar{\nu}_\mu\mu^-$ and $\bar{c}s\nu_\mu\mu^+$, and the same applies to $\tau\nu_\tau\nu_\mu\mu$. Note that the $\mu^-\mu^+\to tb\nu_\mu\mu$ process is not considered in our analysis because the top decay produces more complicated kinematic features, which requires separate studies. Here, we take the $\mu^-\mu^+\to b\bar{b}\nu_\mu\bar{\nu}_\mu$ process as an example, noting

that the following discussion also applies to the other processes to a large extent. As shown in Fig. 1, many diagrams contribute to the $4f$ final states. However, the cross section is dominated by the WW fusion process, particularly when the invariant mass of the $b\bar{b}$ pair is around the Z-pole. For instance, at 10 TeV, the total tree-level cross section of this process is 0.30 pb, whereas that of $\mu^-\mu^+ \to Z\bar{\nu}_\mu\nu_\mu$, $Z \to b\bar{b}$ is approximately 0.29 pb according to MadGraph5 [62]. Furthermore, the diboson process $\mu^-\mu^+ \to ZZ \to \bar{\nu}_\mu\nu_\mu b\bar{b}$ has a considerably smaller cross section, which is approximately 65 ab. Similarly, the irreducible backgrounds $\mu^-\mu^+ \to ZZ \to \bar{\nu}_e\nu_e b\bar{b}/\bar{\nu}_\tau\nu_\tau b\bar{b}$ have negligible rates compared with the signal. Note that in our analysis, we always simulate the full $\mu^-\mu^+ \to 4f$ process, which includes all diagrams except those that involve the Higgs boson, which can be easily removed with an invariant mass window cut around the Higgs mass. The signal events can be selected in experiments by requiring a pair of fermions along with missing momentum in the final states. The backgrounds of this process have considerably smaller rates than the signal one when the invariant mass of the $b\bar{b}$ pair ($M_{b\bar{b}}$) is around the Z-pole. As mentioned earlier, the VBF $\to h \to b\bar{b}$ process can also be efficiently removed with an invariant mass window cut. However, the events with high $b\bar{b}$ invariant mass values are also crucial for our analysis, for which the signal rates are much smaller, and a more careful treatment on the background is required. A potential background process is $\mu^-\mu^+ \to b\bar{b}$ with additional initial-state radiation (ISR) photons, which can fake the signal if the ISR photons are not tagged. This background is highly suppressed when $M_{b\bar{b}}$ is considerably smaller than the c.o.m. energy of the collision. As shown later in Section III, we will impose an upper bound on $M_{b\bar{b}}$ of 1 TeV, which we expect to be able to efficiently remove this background. Another potentially sizable background is $\mu^-\mu^+ \to b\bar{b}\mu^-\mu^+$ via $ZZ/Z\gamma/\gamma\gamma$ fusion with undetected forward muons. Assuming forward muon taggers will be available (see *e.g.,* Refs. [63−65] for more details), only the muons in the very forward regions are undetected; therefore, this background process will have a very small missing transverse momentum ($\not{p}_T$). In contrast, the signal events generally have a sizable $\not{p}_T$. This is illustrated in Fig. 2, where we assume muons with $\eta > 6$ are untagged. Thus, this background can be efficiently removed with a mild $\not{p}_T$ cut (~ 20 GeV). Another potential

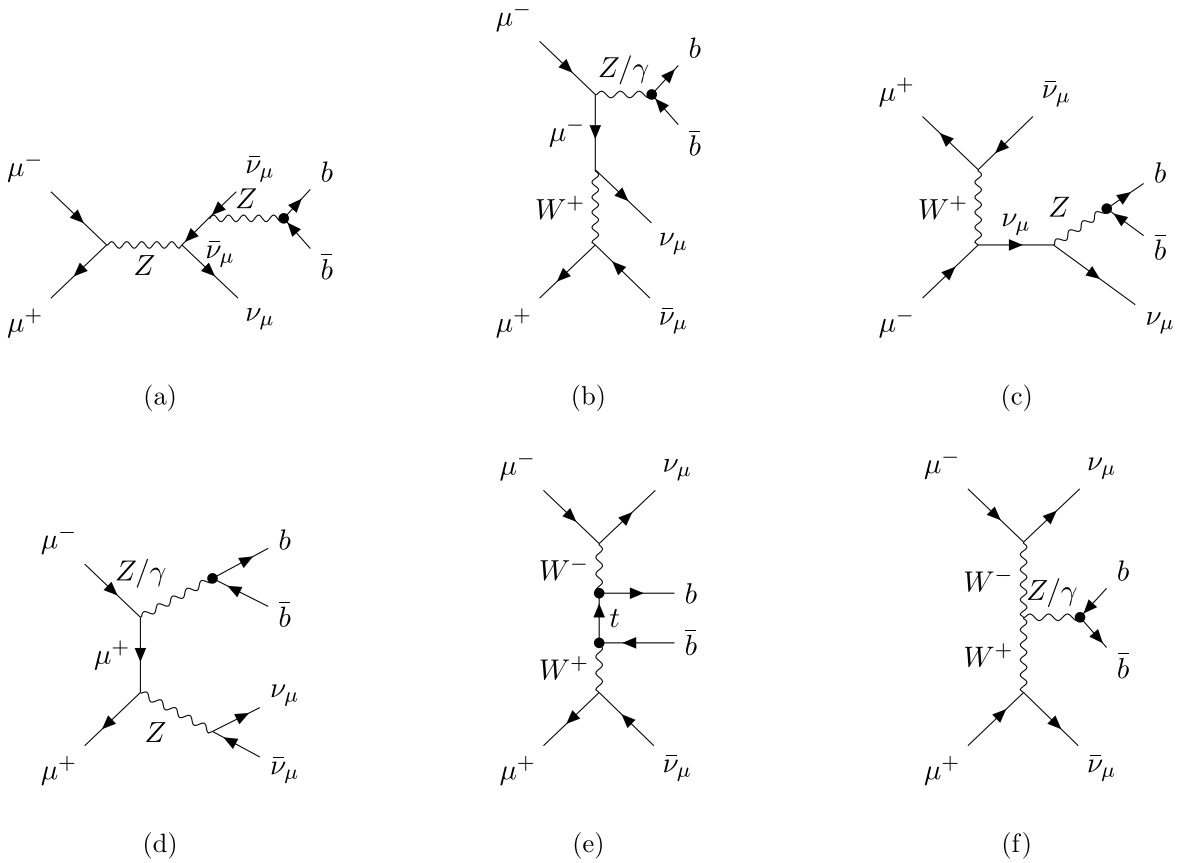

Fig. 1. Typical Feynman diagrams for the process $\mu^-\mu^+ \to b\bar{b}\nu_\mu\bar{\nu}_\mu$. (a) to (c) Examples of $2f \to 2f$ processes with an additional initial or final state Z/γ. Other diagrams of the same type are not explicitly shown. (d) Neutral diboson production. (e) and (f) VBF. BSM vertexes are indicated by black dots.

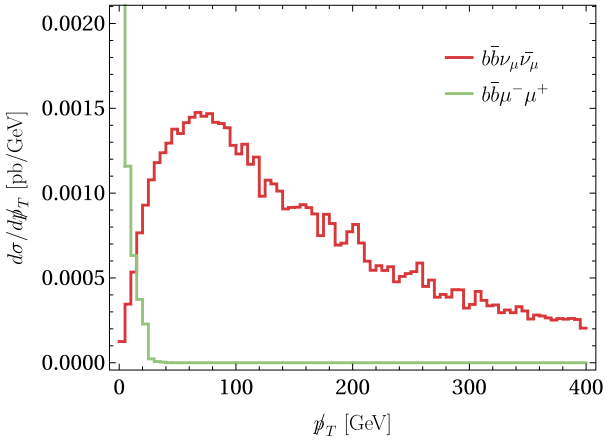

Fig. 2. (color online) Missing transverse momentum ($\not{p}_T$) distribution for $b\bar{b}\nu_\mu\bar{\nu}_\mu$ (red) and $b\bar{b}\mu^-\mu^+$ (green) at $\sqrt{s}$ = 10 TeV. For $b\bar{b}\mu^-\mu^+$, a cut on the muon rapidity of $|\eta_\mu| > 6$ is imposed, corresponding to both muons being untagged.

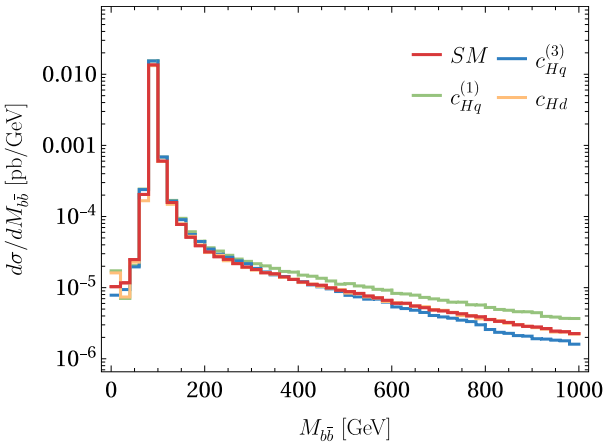

Fig. 3. (color online) Differential cross section distribution on the invariant mass of $b\bar{b}$ pair ($M_{b\bar{b}}$) for the $\mu^-\mu^+ \to b\bar{b}\nu_\mu\bar{\nu}_\mu$ process with $\sqrt{s} = 10$ TeV. A bin width of 20 GeV is selected. The red curve corresponds to the SM value, whereas the other three curves each correspond to one of the three Wilson coefficients $c_{Hq}^{(1)}, c_{Hq}^{(3)}, c_{Hd}$ set to a reference value of 1 (with $\Lambda = 1$ TeV), whereas the other two are set to zero. Note that the low energy bins (with $M_{b\bar{b}} \ll m_Z$) are subject to large statistical uncertainties in our simulation.

background is the QCD parton induced di-jet backgrounds [66, 67], which we also expect to be efficiently removed with this $\not{p}_T$ cut. For convenience, we omit these background processes in our analysis and leave a more detailed background analysis to future studies.

The differential distribution of the $\mu^-\mu^+ \to b\bar{b}\nu_\mu\bar{\nu}_\mu$ process contains crucial information. In Fig. 3, we show the binned differential cross section as a function of the invariant mass of the $b\bar{b}$ pair. The red curve corresponds to the SM value, whereas the other three curves each correspond to one of the three Wilson coefficients $c_{Hq}^{(1)}, c_{Hq}^{(3)}, c_{Hd}$ set to a reference value of 1 (with $\Lambda = 1$ TeV), and the other two are set to zero. A peak around the Z-pole can be clearly observed, which corresponds to the s-channel Z diagram in Fig. 1(f). The cross section also decreases rapidly as the invariant mass increases – a typical feature for the WW fusion processes. Nevertheless, the events with high invariant mass contain important information that is complementary to those around the Z-pole. In particular, as shown in Fig. 3, the cross section becomes more sensitive to the coefficients $c_{Hq}^{(1)}$ and $c_{Hq}^{(3)}$ at higher invariant mass, a feature expected from their energy enhancements. As we will show later, a binned analysis that considers the information in the invariant mass distribution makes it possible to simultaneously constrain all three Wilson coefficients.

The angular distributions of the $\mu^-\mu^+ \to b\bar{b}\nu_\mu\bar{\nu}_\mu$ process also contain useful information. For instance, the diagram with the s-channel Z would have different kinematics compared to the one with a t-channel fermion exchange. Ideally, this information is captured by the angle between the incoming $W^\pm$ and the outgoing b or $\bar{b}$. However, this angle cannot be directly measured owing to the missing neutrinos. Nevertheless, part of the information is still in the production polar angles of b and $\bar{b}$. In Fig. 4, we show the distribution of the variable $|\cos\bar{\theta}|$ for events in different ranges of $M_{b\bar{b}}$ (same as the choices of nine bins listed in Table 2), where θ is the polar angle of b in the c.o.m. frame of the $b\bar{b}$ system. The reason for selecting the $b\bar{b}$ c.o.m. frame is that the kinematics in the lab frame are subject to a large longitudinal boost, similar to the situation at the LHC. Note that, in the $b\bar{b}$ c.o.m. frame, the incoming μ^- and μ^+ are generally not on the same line, and $|\cos\bar{\theta}|$ is simply defined as the average of the two different values,

$$|\cos\bar{\theta}| \equiv \frac{1}{2}\left(\left|\cos\theta_{\mu^- b}\right| + \left|\cos\theta_{\mu^+ b}\right|\right), \tag{9}$$

where $\theta_{\mu^- b}$ ($\theta_{\mu^+ b}$) is the angle between μ^- (μ^+) and b. Here, for the three Wilson coefficients $c_{Hq}^{(1)}, c_{Hq}^{(3)}, c_{Hd}$, a reference value of 10 is selected instead (assuming $\Lambda = 1$ TeV, and in each case, the other two are set to zero) to better visualize their effects [1]. Figure 4 shows that, for a large $M_{b\bar{b}}$ (well above the Z pole), $|\cos\bar{\theta}|$ is sensitive to $c_{Hq}^{(1)}$ and $c_{Hq}^{(3)}$, which provide a more even distribution, whereas the SM distribution concentrates more in the forward region (because the SM cross section is dominated by the t-channel diagram at high $M_{b\bar{b}}$). Thus, for a large $M_{b\bar{b}}$, we can further use the $|\cos\bar{\theta}|$ distribution to increase

1) We also consider only linear contributions of the Wilson coefficients. Note that in the analysis the typical constraints on the Wilson coefficients are much smaller than 10, and their quadratic contributions are negligible.

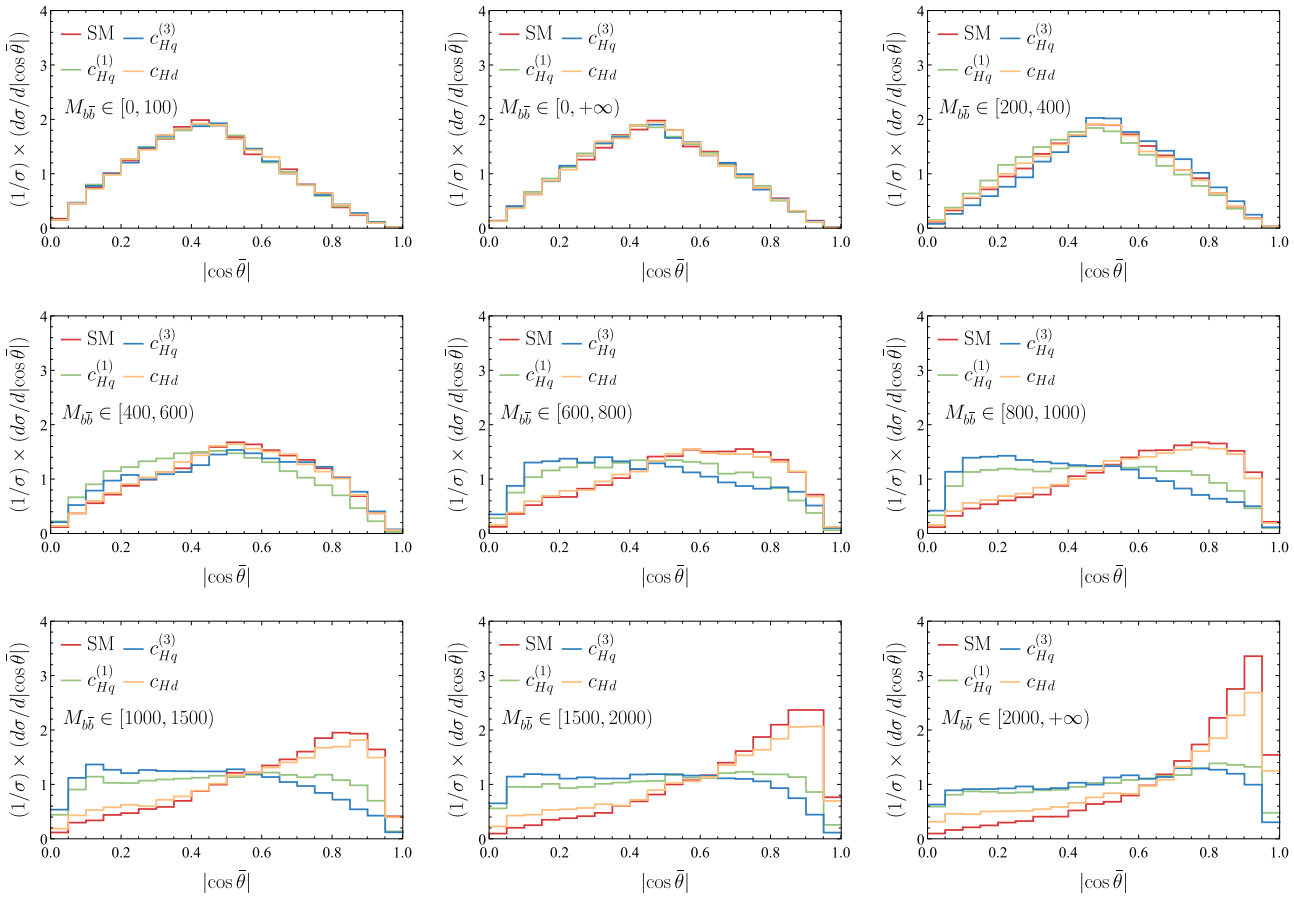

Fig. 4. (color online) Differential cross section of the $|\cos\bar{\theta}|$ variable, defined as $|\cos\bar{\theta}| \equiv \frac{1}{2}\left(\left|\cos\theta_{\mu^- b}\right| + \left|\cos\theta_{\mu^+ b}\right|\right)$, where $\theta_{\mu^- b}$ ($\theta_{\mu^+ b}$) is the angle between μ^- (μ^+) and b in the c.o.m. frame of the $b\bar{b}$ system. A reference value of 10 is selected here for each Wilson coefficient (assuming $\Lambda = 1$ TeV, and setting the other two to zero), with only the linear contribution considered. The bin width is selected to be 0.05. A (different) invariant mass selection is applied for each of the nine plots, corresponding to the nine bins listed in Table 2.

the sensitivity to the Wilson coefficients.

The discussion above also applies to the $\mu^-\mu^+ \to c\bar{c}\nu_\mu\bar{\nu}_\mu$ and $\mu^-\mu^+ \to \tau^-\tau^+\nu_\mu\bar{\nu}_\mu$, which have very similar features. For the asymmetric processes $\mu^-\mu^+ \to cs\nu_\mu\mu$ and $\mu^-\mu^+ \to \tau\nu_\tau\nu_\mu\mu$, the scenarios are slightly different. Taking $\tau\nu_\tau\nu_\mu\mu$ as an example, the typical diagrams are shown in Fig. 5, where the dominant contribution to the total cross section comes from the $WZ/W\gamma$ fusion diagrams (f), (g) [1)]. These processes are also more sensitive to the $O_{Hl}^{(3)}$ ($O_{Hq}^{(3)}$ for $cs\nu_\mu\mu$) operator, which modifies the W-fermion couplings. Again, we do not expect any significant background for this process. While the invariant mass distribution of the $\tau\nu_\tau$ pair still contains useful information and peaks around the W mass, it cannot be reconstructed owing to the additional missing ν_μ. Nevertheless, the measurement of the total rate of this process contains useful information, which is complementary to that of $\mu^-\mu^+ \to \tau^-\tau^+\nu_\mu\bar{\nu}_\mu$, as we will show later. Similarly, the measurement of $cs\nu_\mu\mu$ process also provides information complementary to that of $c\bar{c}\nu_\mu\bar{\nu}_\mu$.

III. MEASUREMENTS AND ANALYSES

A. Run scenarios

We consider two runs with c.o.m. energies of 10 and 30 TeV. The reference values of the integrated luminosity are taken from the ideal luminosity relations [3],

$$\mathcal{L}_{\rm int} = 10\ {\rm ab}^{-1}\left(\frac{E_{\rm cm}}{10\ {\rm TeV}}\right)^2, \tag{10}$$

which are $10\,{\rm ab}^{-1}$ for the 10 TeV run and $90\,{\rm ab}^{-1}$ for the 30 TeV run. Note that the run scenarios considered in this

1) Note that, while the diboson process in Fig. 5 (d) and (e) is very sensitive to a number of operators, in our analysis the only SMEFT contribution is the modification of the $W\tau\nu_\tau$ coupling, in which case the diboson process plays a less important row due to its smaller cross section. Once again, all diagrams to the same $4f$ final states are included in our analysis.

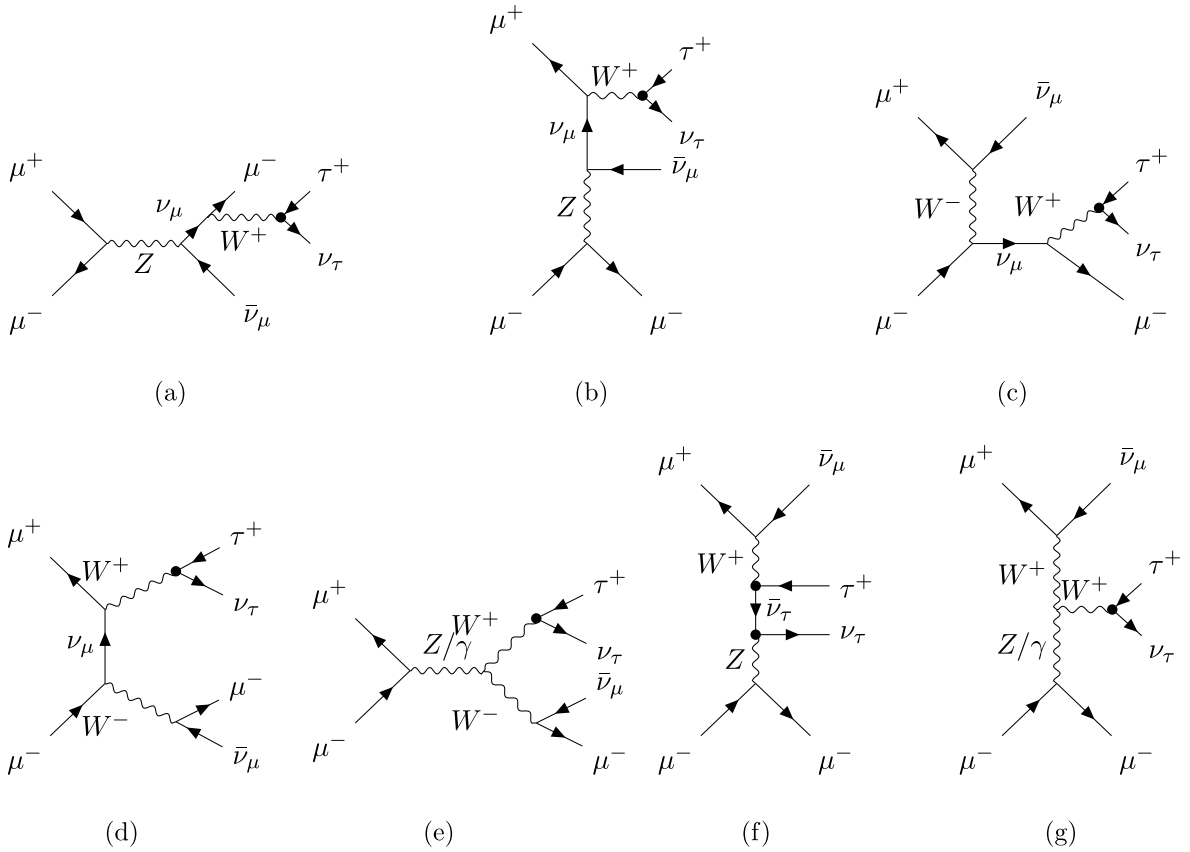

Fig. 5. Typical Feynman diagram for the process $\mu^-\mu^+ \to \tau^+\nu_\tau\bar{\nu}_\mu\mu^-$. (a) to (c) Examples of $2f \to 2f$ processes with additional W in the initial or final state; (d) and (e) diboson production; (f) and (g) VBF. BSM vertexes are indicated by black dots.

study are optimistic and may change with the continuous development of the muon collider R&D program.

B. Methodology

We simulate our signal processes with MADGRAPH5_AMC@NLO v3.5.6 [68] at the parton level with SMEFT effects implemented using the SMEFTsim 3.0 package [69] as a UFO model [70]. We apply the following cuts within this study: $p_T^j > 20\,\text{GeV}$ and $|\eta_j| < 2.44$ for jets, and $p_T^l > 10\,\text{GeV}$, $|\eta_\tau| < 2.44$, and $|\eta_\mu| < 6$ for charged leptons [65−67]. The choices of rapidity cuts are typical for the analyses at muon colliders, because detecting jets and charged leptons (except muon) close to the beam is difficult owing to the dramatic beam induced background (BIB) [65]. We also assume that forward muon taggers [63−65] are implemented, which results in the considerably larger acceptance for η_μ. We do not expect these cuts to have very significant impacts on our analysis except for the asymmetric processes $cs\nu_\mu\mu$ and $\tau\nu_\tau\nu_\mu\mu$, for which we require the muon to be tagged. Thus, the selection efficiency of the asymmetric processes is highly sensitive to the performance of the forward muon taggers. We do not expect the detector effects to have a significant impact in our analysis either, as we use only simple kinematic variables including the invariant mass and the $|\cos\bar{\theta}|$ variable defined in Eq. (9). However, the tagging efficiencies of b, c, and τ are crucial in our analysis because they have a direct impact on the total rate. Ref. [3] provides a benchmark efficiency of approximately 80% for tagging one b jet and approximately 70% for the di-tau system. For the charm and strange quarks, the tagging efficiencies are not listed in Ref. [3], so we use the recent CEPC study [71] as a reference (assuming a muon collider can achieve similar performance). These efficiencies are approximately 70% for a charm jet and 50% for a strange jet[1)]. Note that, these tagging rates can be somewhat optimistic for muon colliders and should be replaced by more realistic estimations in future studies when they become available. In addition to the $\tau\nu_\tau\nu_\mu\mu$ process, we always require both final state fermions to be tagged, which yields, *e.g.*, a 64% efficiency for the $b\bar{b}$ pair. For $\tau\nu_\tau\nu_\mu\mu$, we assume that the final states can be selected by requiring one τ-tag in addition to a muon and missing momentum and naively assign an efficiency of $\sqrt{0.7} \approx 0.84$. We do not require the discrimination between b and $\bar{b}$ (or c and $\bar{c}$) because this

1) For the charm-tagging rate, Refs. [15, 72] suggest a reference value of around 67% for CLIC, which is close to 70%.

information is not used in our analysis. The signal selection efficiencies based on tagging are summarized in Table 1. We also do not expect mis-tagging to have a significant impact on our analyses because we do not have any overwhelming backgrounds to start with. The only sizable mis-tagging rate is that for b to be identified as c, which is approximately 20% [3]. Because we require both final state quarks to be tagged, we only expect a small mixing ($\lesssim 4\%$) between different signal events, which we simply ignore in our study. When all the mis-tagging rates are available, we can also implement their effects on the signal events (which becomes a mixture of different processes) under a global SMEFT framework, which is beyond the scope of our current analysis.

We consider the leading SMEFT contributions at the Λ^{-2} order. At the cross section level, this means that only the linear contributions of the Wilson coefficients are considered, whereas the quadratic contributions are omitted because they are at the Λ^{-4}order. Given the high measurement precision, this is a very good approximation in our analysis. Thus, the SMEFT predictions of the cross sections are parameterized as

$$\sigma_{\rm SMEFT} = \sigma_{\rm SM} + \sum_i \alpha_i c_i + O(\Lambda^{-4}), \tag{11}$$

where the coefficients α_i can be determined numerically from the MC simulation. The full list of the numerical expressions of Eq. (11) for all the processes and bins are provided in Appendix A. To extract the bounds on the Wilson coefficients, we implement the chi-squared method, with the total χ^2 given by

$$\chi^2 = \sum_i^{\rm bins} \frac{(\sigma_{i,\rm SMEFT} - \sigma_{i,\rm exp})^2}{(\Delta\sigma_i)^2}, \tag{12}$$

where the sum is performed over all the bins (to be specified later), and $\sigma_{i,\rm SMEFT}$, $\sigma_{i,\rm exp}$, and $\Delta\sigma_i$ are the SMEFT prediction, measured central value, and (one-sigma) uncertainty of the cross section in the ith bin, respectively. By construction, we assume the measured central values are SM-like, $\sigma_{i,\rm exp} = \sigma_{i,\rm SM}$. Note that we have also explicitly assumed that the measurements of different bins are uncorrelated. We consider only statistical uncertainties, in which case

$$\Delta\sigma_i = \frac{\sigma_{i,\rm SM}}{\sqrt{N_{i,\rm SM}}} = \sqrt{\frac{\sigma_{i,\rm SM}}{L}}, \tag{13}$$

where $N_{i,\rm SM}$ is the number of events in the bin, and L is the total luminosity.

The inverse of covariant matrix of the Wilson coefficients can be estimated as

$$(U^{-1})_{ij} = \frac{1}{2}\frac{\partial^2\chi^2}{\partial c_i \partial c_j}\bigg|_{c=\hat{c}}, \tag{14}$$

where c_i are the Wilson coefficients and $\hat{c}$ their best fitted values (with a minimum χ^2), which are zero in our analysis by construction. The one sigma bounds δc_i and correlation matrix ρ_{ij} of the Wilson coefficients can be obtained as

$$\delta c_i = \sqrt{U_{ii}}, \tag{15}$$

and

$$\rho_{ij} = \frac{U_{ij}}{\delta c_i \delta c_j}. \tag{16}$$

Table 1. Summary of the tagging efficiencies of different processes implemented in our analysis.

Process	Requirement	Efficiency
$\mu^-\mu^+ \to b\bar{b}\nu_\mu\bar{\nu}_\mu$	2 b-tags	0.64
$\mu^-\mu^+ \to c\bar{c}\nu_\mu\bar{\nu}_\mu$	2 c-tags	0.49
$\mu^-\mu^+ \to \tau^-\tau^+\nu_\mu\bar{\nu}_\mu$	2 τ-tags	0.7
$\mu^-\mu^+ \to cs\nu_\mu\mu$	1 c-tag and 1 s-tag	0.35
$\mu^-\mu^+ \to \tau\nu_\tau\nu_\mu\mu$	1 τ-tag	0.84

C. Binning

For the symmetric processes ($\mu^-\mu^+ \to f\bar{f}\nu_\mu\bar{\nu}_\mu$ where $f\bar{f} = b\bar{b}$, $c\bar{c}$, or $\tau^-\tau^+$), the invariant mass distribution of the $f\bar{f}$ pair contains crucial information for probing the Wilson coefficients. To extract this information, we perform a binned analysis by dividing the signal process into nine bins, with the range of the bins listed in Table 2. The first bin has the largest cross section owing to the Z resonance. To ensure sufficient MC statistics for higher invariant mass bins, each bin is separately generated in MadGraph with the corresponding invariant mass cuts.

As mentioned earlier, for very high invariant mass, the signal may be subject to a sizable $\mu^-\mu^+ \to f\bar{f}$ background, and imposing a upper bound on $M_{f\bar{f}}$ is desirable. Furthermore, the validity of the EFT analysis also tends to be problematic for a high $M_{f\bar{f}}$, given that the typical reach on the new physics scale Λ could be comparable or even smaller than $M_{f\bar{f}}$ [73, 74]. To resolve both issues, after we study the effects of the invariant mass bins in Section IV.A, we will impose an upper bound of 1 TeV on $M_{f\bar{f}}$ and discard bins 7-9 listed in Table 2.

In addition, we also utilize the $|\cos\bar{\theta}|$ variable in Eq. (9). To capture the essential information shown in Fig. 4, we further divide the events in each invariant mass bin

Table 2. Binning of the invariant mass of the $f\bar{f}$ pair for $\mu^-\mu^+ \to f\bar{f}\nu_\mu\bar{\nu}_\mu$, where $f\bar{f} = b\bar{b}$, $c\bar{c}$, or $\tau^-\tau^+$. Note that for all results, except those in Section IV.A, we will impose the cut $M_{f\bar{f}} < 1$ TeV and discard bins 7-9.

Bin number	bin 1	bin 2	bin 3	bin 4	bin 5	bin 6	bin 7	bin 8	bin 9
Invariant mass/GeV	[0, 100)	[100, 200)	[200, 400)	[400, 600)	[600, 800)	[800, 1000)	[1000, 1500)	[1500, 2000)	[2000, +∞)

Table 3. Division point of observable $|\cos\bar{\theta}|$ (defined in Eq. (9)) for different processes and collision energies. For each listed invariant mass bin, the events are further divided into two bins with $|\cos\bar{\theta}| < x$ and $|\cos\bar{\theta}| > x$, where x is the division point.

Invariant Mass	$b\bar{b}$		$c\bar{c}$		$\tau^-\tau^+$	
/GeV	10 TeV	30 TeV	10 TeV	30 TeV	10 TeV	30 TeV
[600, 800)	0.45	0.5	0.45	0.45	0.5	0.5
[800, 1000)	0.55	0.5	0.45	0.45	0.5	0.5
[1000, 1500)	0.6	0.5	0.45	0.5	0.6	0.55
[1500, 2000)	0.65	0.6	0.5	0.5	0.7	0.5
[2000, +∞)	0.7	0.65	0.6	0.6	0.75	0.6

starting from 600 GeV into two bins, with the division point as listed in Table 3. The values of the division points are determined based a simple optimization procedure (by examining a few benchmark values and selecting the one with the best result). Finally, the total χ^2 is obtained by summing over the χ^2 values of all bins using Eq. (12). As shown in the next section, binning is very useful in discriminating the contributions of different Wilson coefficients and can significantly improve the overall results.

For the asymmetric processes ($\mu^-\mu^+ \to cs\nu_\mu\mu$, $\mu^-\mu^+ \to \tau\nu_\tau\nu_\mu\mu$), we consider only the measurement of the total cross section and combine its χ^2 with that of the corresponding symmetric process. This also brings a nontrivial improvement on the top of the symmetric process, as shown in the next section. Note that, similar to the symmetric processes, here the events with high invariant masses are also potentially subject to EFT validity problems. For $\mu^-\mu^+ \to \tau\nu_\tau\nu_\mu\mu$ in particular, removing these events is nontrivial because $M_{\tau\nu_\tau}$ cannot be directly measured. Nevertheless, because we use only the total rates of the asymmetric processes, we do not expect the events with high invariant masses to have a significant impact on our study. A more careful treatment on the differential distributions of the asymmetric processes is left for future studies.

IV. RESULTS

Our fit results are presented in this section. In Sections IV.A and IV.B, we consider the impacts of binning on the invariant mass and $|\cos\bar{\theta}|$, using $\mu^-\mu^+ \to b\bar{b}\nu_\mu\bar{\nu}_\mu$ as an example. In Section IV.C, we compare the results from the $\mu^-\mu^+ \to \tau^-\tau^+\nu_\mu\bar{\nu}_\mu$ process alone with those that also include the $\tau\nu_\tau\nu_\mu\mu$ process, where the latter provides a sizable improvement. Finally, a summary of the reaches on all Wilson coefficients is provided in Section IV.D. Note that, for the results in Sections IV.A, IV.B, and IV.C, we have omitted the flavor indices of the Wilson coefficients, which are 33 (diagonal, third generation). The flavor indices are restored in Section IV.D. Additional results are provided in Appendix B.

A. Impacts of the invariant mass bins

To illustrate the impacts of different invariant mass bins, Fig. 6 shows the $\Delta\chi^2 = 1$ contours [1] of the three-parameter $(c_{Hq}^{(1)}, c_{Hq}^{(3)}, c_{Hd})$ fit of the process $\mu^-\mu^+ \to b\bar{b}\nu_\mu\bar{\nu}_\mu$ for both the 10 TeV run (top row) and 30 TeV run (bottom row). In each case, we divide the invariant mass bins into three groups (bins 1-3, 4-6, and 7-9), and the $\Delta\chi^2 = 1$ contours are shown separately for each group of three bins, which are projected on three different 2D planes of the three parameters. The $|\cos\bar{\theta}|$ variable is not considered here. Note that, without binning (which is essentially the same as including only the first bin because the cross section is dominated by the Z resonance), the cross section measurement provides only one constraint on the three parameters. A combination of at least three different bins is required to simultaneously constrain all three parameters. Among the three groups of bins, bins 1-3 clearly provide the best constraints owing to the large rates around the Z pole. The results from higher invariant mass bins alone are generally worse, and they also suffer from large (approximate) flat directions. Nevertheless, the high invariant mass bins carry important complementary information to those of the Z-resonance events. This is made clearer in Fig. 7, where we present the same set of results, but for combinations of bins 1-3, 1-6, and 1-9.

1) Note that $\Delta\chi^2 = \chi^2 - \chi^2_{\rm min}$, where $\chi^2_{\rm min} = \chi^2(c_i = 0) = 0$ by our assumption that all measurements are SM like.

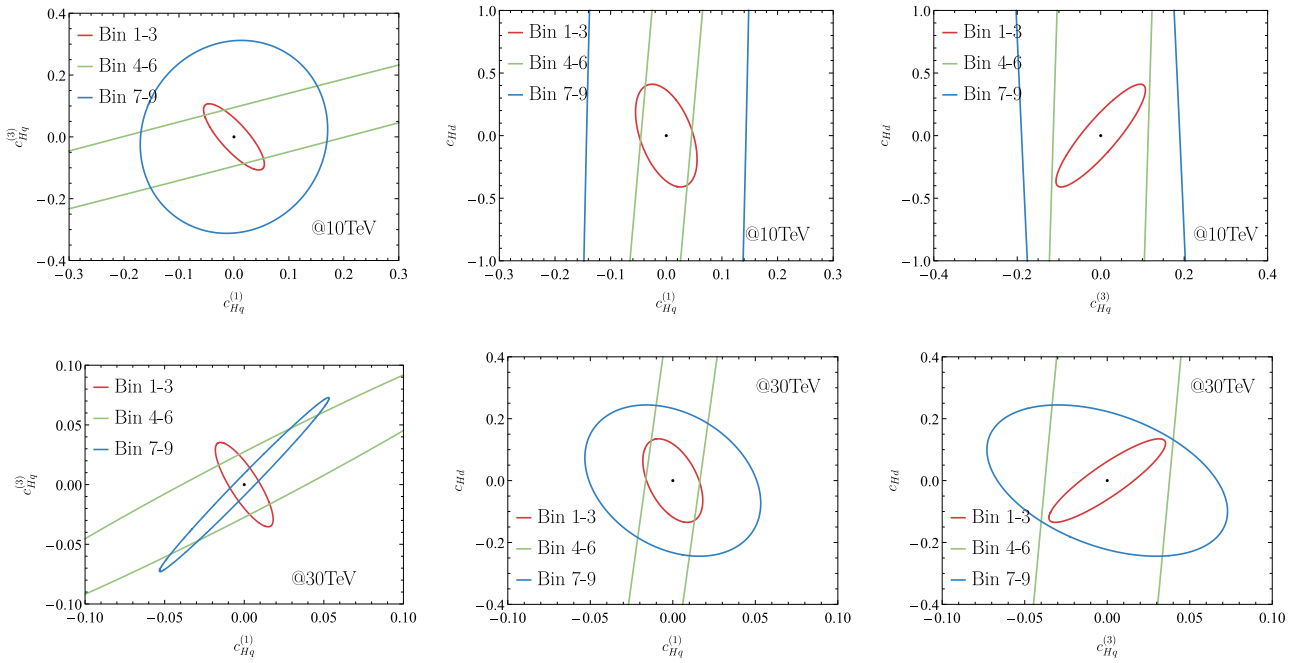

Fig. 6. (color online) $\Delta\chi^2 = 1$ contours from the three-parameter $(c_{Hq}^{(1)}, c_{Hq}^{(3)}, c_{Hd})$ fit to $\mu^-\mu^+ \to b\bar{b}\nu_\mu\bar{\nu}_\mu$ at 10 TeV (top row) and 30 TeV (bottom row), obtained from three separate groups of invariant mass bins as listed in Table 2. These groups correspond to bins 1-3 (red contours), bins 4-6 (green contours), and bins 7-9 (blue contours). For each row, the results are projected onto three 2D planes (each with the other parameter marginalized). We set $\Lambda = 1$ TeV for convenience.

This clearly demonstrates the improvements introduced by the higher invariant mass bins on top of those around the Z pole. As mentioned earlier, we will discard the signal events with invariant mass larger than 1 TeV (bins 7-9) to reduce the background and improve EFT validity. While this would reduce the overall reach, Fig. 7 shows that the impact of this cut is under control given that reaches with bins 1-6 (green contours) are not much worse than the ones with all the bins (blue contours).

The results for $\mu^-\mu^+ \to c\bar{c}\nu_\mu\bar{\nu}_\mu$ and $\mu^-\mu^+ \to \tau^-\tau^+\nu_\mu\bar{\nu}_\mu$ are shown in Fig. B1 and Fig. B2 in Appendix B, respectively, which exhibit similar features.

B. Impacts of the $|\cos\bar{\theta}|$ bins

In addition to the invariant mass bins, we consider the impacts of further splitting the high invariant mass bins ($M_{b\bar{b}} > 600$ GeV) in $|\cos\bar{\theta}|$ as in Table 3. In Fig. 8, we compare the results that include only invariant mass bins ($M_{b\bar{b}}$, dashed contours) and the results that further split the bins in $|\cos\bar{\theta}|$ ($M_{b\bar{b}}$ & $|\cos\bar{\theta}|$, solid contours). Although the improvements from the binning in $|\cos\bar{\theta}|$ are relatively small in all cases, they are still visible, particularly for the 10 TeV case. In Appendix B, similar results can be found in Fig. B3 for $\mu^-\mu^+ \to c\bar{c}\nu_\mu\bar{\nu}_\mu$ and Fig. B4 for $\mu^-\mu^+ \to \tau^-\tau^+\nu_\mu\bar{\nu}_\mu$.

C. Impacts of the asymmetric processes

In addition to the full binned analysis of the symmetric process, the inclusion of the asymmetric process may provide additional improvement. Note that in our study, we do not consider the asymmetric process of $\mu^-\mu^+ \to b\bar{b}\nu_\mu\bar{\nu}_\mu$, which is $\mu^-\mu^+ \to tb\mu\nu_\mu$, owing to the complexity of the top decay. Instead, we compare $\mu^-\mu^+ \to \tau^-\tau^+\nu_\mu\bar{\nu}_\mu$ and $\mu^-\mu^+ \to \tau\nu_\tau\nu_\mu\mu$, with the results shown in Fig. 9. The combination of the two processes ($\tau^+\tau^-$ & $\tau\nu_\tau$, solid contour) provides a sizable improvement to the top of the symmetric process alone ($\tau^+\tau^-$ only, dashed contour), particulary for the 10 TeV run. The improvement is most significant for $c_{Hl}^{(3)}$, which modifies the W-fermion couplings. As mentioned in Section III.B, we have imposed a rapidity cut of $|\eta_\mu| < 6$ on muons, assuming forward muon taggers [63–65] will be implemented. Without forward muon taggers, the asymmetric processes could suffer from a considerably smaller signal selection efficiency. Thus, our analysis provides an important case that motivates the implementation of forward muon taggers.

Similar results for the combination of the processes $\mu^-\mu^+ \to c\bar{c}\nu_\mu\bar{\nu}_\mu$ and $\mu^-\mu^+ \to cs\nu_\mu\mu$ are shown in Fig. B5 in Appendix B, which also exhibits a significant improvement for $c_{Hq}^{(3)}$.

D. Constraints on the Wilson coefficients

A summary of the reaches on all the Wilson coefficients considered in our analysis is presented in Fig. 10. The measurements of all the processes in Table 1 are considered, whereas for the symmetric processes, the bin-

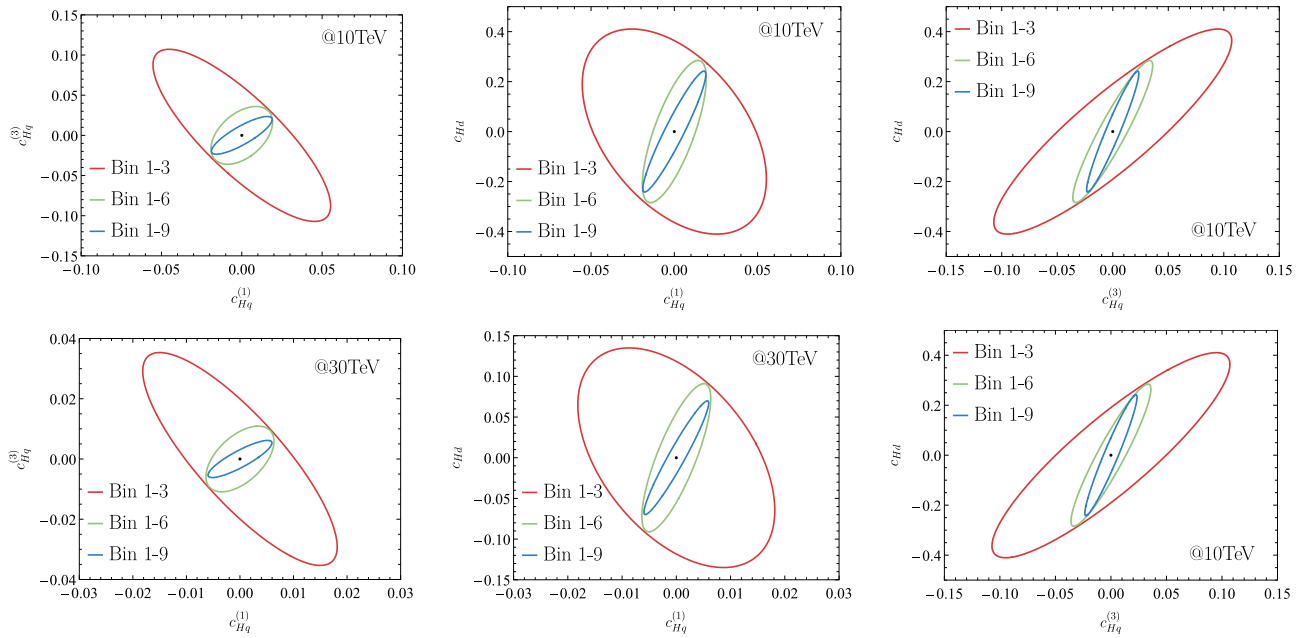

Fig. 7. (color online) $\Delta\chi^2 = 1$ contours from the three-parameter $(c_{Hq}^{(1)}, c_{Hq}^{(3)}, c_{Hd})$ fit to $\mu^-\mu^+ \to b\bar{b}\nu_\mu\bar{\nu}_\mu$ at 10 TeV (top row) and 30 TeV (bottom row), with the invariant mass bins in Table 2. For each row, the results are projected onto three 2D planes (each with the other parameter marginalized). The contours with the first three, six, and all nine bins are shown. We set $\Lambda = 1$ TeV for convenience.

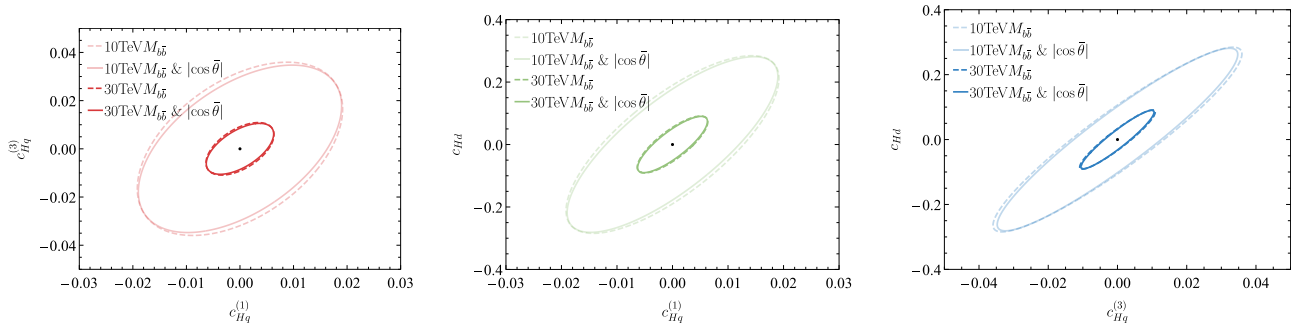

Fig. 8. (color online) Comparison of the results for $\mu^-\mu^+ \to b\bar{b}\nu_\mu\bar{\nu}_\mu$ with only the invariant mass bins (dashed contours, binning as in Table 2) and also with the $|\cos\bar{\theta}|$ bins (solid contours, binning as in Table 3). An invariant mass cut of $M_{b\bar{b}} < 1$ TeV is imposed. The contours correspond to $\Delta\chi^2 = 1$ from the three-parameter $(c_{Hq}^{(1)}, c_{Hq}^{(3)}, c_{Hd})$ fit. We set $\Lambda = 1$ TeV for convenience.

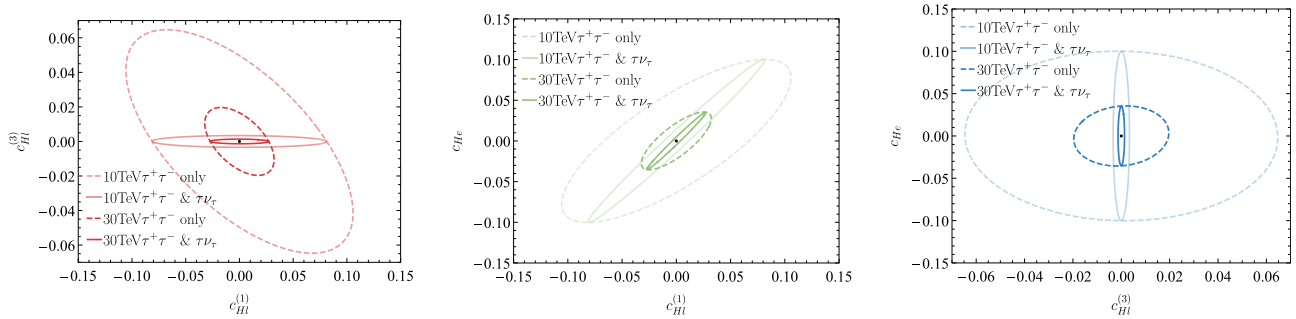

Fig. 9. (color online) Comparison of the results for the three parameters $c_{Hl}^{(1)}, c_{Hl}^{(3)}, c_{He}$ (all with flavor indices 33) from the measurements of $\mu^-\mu^+ \to \tau^-\tau^+\nu_\mu\bar{\nu}_\mu$ only (labeled as "$\tau^+\tau^-$ only", dashed contours, with $M_{\tau^+\tau^-} < 1$ TeV) and the combination of $\mu^-\mu^+ \to \tau^-\tau^+\nu_\mu\bar{\nu}_\mu$ and $\mu^-\mu^+ \to \tau\nu_\tau\nu_\mu\mu$ (labeled as "$\tau^+\tau^-\&\tau\nu_\tau$", solid contours). Contours correspond to $\Delta\chi^2 = 1$. We set $\Lambda = 1$ TeV for convenience.

ning is performed with both the invariant mass of the fermion pair (as in Table 2) and the $|\cos\bar{\theta}|$ variable (Table 3). Note again that we have imposed an invariant mass cut of $M_{f\bar{f}} < 1$ TeV to reduce the background and improve EFT validity. The previously omitted flavor indices are also explicitly shown in Fig. 10. Both the global-fit results (in our case, which involve three operators for any given process) and the individual ones (by switching on one operator at a time) are shown.

For comparison, we also show in Fig. 10 the reach of CEPC from a Higgs+EW global fit, converted from the results in Ref. [43] to the basis in Ref. [29]. Note that the results in Ref. [43] are obtained under a different framework with more parameters and measurements included (with all the other parameters marginalized here); therefore, a direct comparison under the same conditions is not possible. Furthermore, we have excluded the CEPC $t\bar{t}$ measurements (hence the bounds on $(c_{Hq}^{(1)})_{33}$ and $(c_{Hq}^{(3)})_{33}$ are missing) because the top measurements at a muon collider are also excluded in our analysis. Nevertheless, we observe that the overall reach of the muon collider on these Wilson coefficients is generally on the same order as those at the CEPC (or FCC-ee).

The numerical values of the one-sigma bounds of the Wilson coefficients and their correlation matrices are listed in Tables 4, 5, and 6.

V. CONCLUSION

In this study, we consider the measurements of several vector-boson-fusion-to-two-fermions (VBF$\to 2f$, with an additional $\bar{\nu}_\mu\nu_\mu$ or $\nu_\mu\mu$ pair) processes at a future high

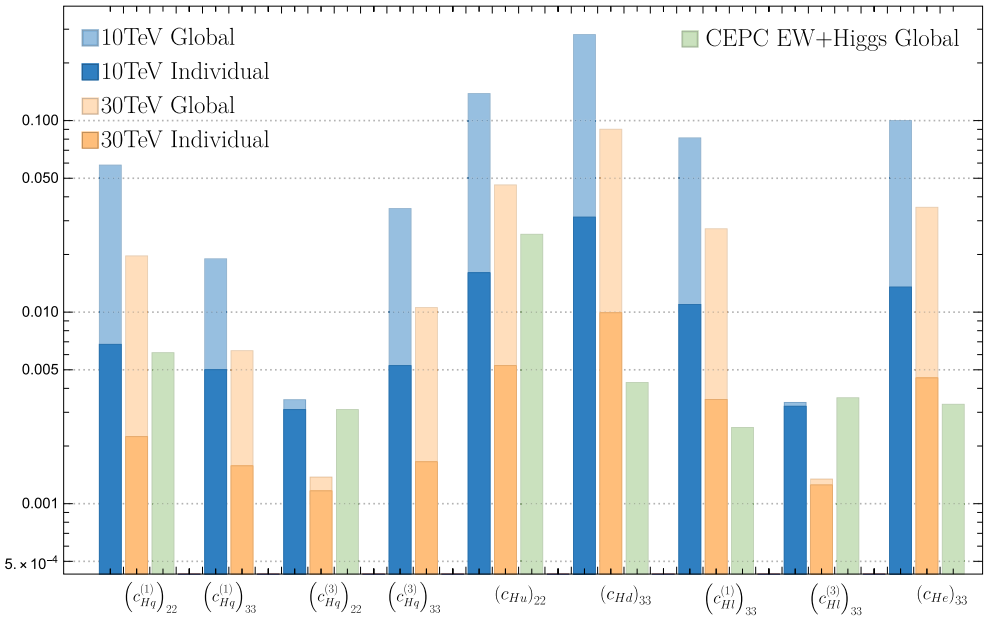

Fig. 10. (color online) 1 σ constraints on Wilson coefficients in our analysis. The light-shaded bars correspond to global-fit results, whereas the solid bars are individual fit results. The blue (orange) bars correspond to the results in the 10 (30) TeV run. The CEPC results from a full EW+Higgs global fit are shown as green bars, which have been converted from the results in Ref. [43]. We set $\Lambda = 1$ TeV for convenience.

Table 4. One-sigma individual and global bounds of $(c_{Hq}^{(1)})_{33}$, $(c_{Hq}^{(3)})_{33}$, and $(c_{Hd})_{33}$ and their correlations (corresponding to the global bounds) from the measurement of $\mu^-\mu^+ \to b\bar{b}\nu_\mu\bar{\nu}_\mu$ in the 10 TeV run (left panel) and 30 TeV run (right panel). An invariant mass cut of $M_{f\bar{f}} < 1$ TeV is imposed, after which all the invariant mass and $|\cos\bar{\theta}|$ bins are included. We set $\Lambda = 1$ TeV for convenience.

	10 TeV						30 TeV					
	68%CL 1σ bound ($\times 10^{-2}$)		Correlation matrix				68%CL 1σ bound ($\times 10^{-2}$)		Correlation matrix			
	Individual	Global	$(c_{Hq}^{(1)})_{33}$	$(c_{Hq}^{(3)})_{33}$	$(c_{Hd})_{33}$		Individual	Global	$(c_{Hq}^{(1)})_{33}$	$(c_{Hq}^{(3)})_{33}$	$(c_{Hd})_{33}$	
$(c_{Hq}^{(1)})_{33}$	±0.500	±1.90	1			$(c_{Hq}^{(1)})_{33}$	±0.158	±0.629	1			
$(c_{Hq}^{(3)})_{33}$	±0.526	±3.47	0.871	1		$(c_{Hq}^{(3)})_{33}$	±0.165	±1.06	0.895	1		
$(c_{Hd})_{33}$	±3.14	±28.1	0.954	0.963	1	$(c_{Hd})_{33}$	±0.992	±9.01	0.966	0.961	1	

Table 5. Same as Table 4 but for $\left(c_{Hq}^{(1)}\right)_{22}$, $\left(c_{Hq}^{(3)}\right)_{22}$, and $(c_{Hu})_{22}$ from the measurements of $\mu^-\mu^+ \to c\bar{c}\nu_\mu\bar{\nu}_\mu$ and $\mu^-\mu^+ \to cs\nu_\mu\mu$.

	10 TeV						30 TeV					
	68%CL 1σ bound ($\times10^{-2}$)		Correlation matrix				68%CL 1σ bound ($\times10^{-2}$)		Correlation matrix			
	Individual	Global	$\left(c_{Hq}^{(1)}\right)_{22}$	$\left(c_{Hq}^{(3)}\right)_{22}$	$(c_{Hu})_{22}$		Individual	Global	$\left(c_{Hq}^{(1)}\right)_{22}$	$\left(c_{Hq}^{(3)}\right)_{22}$	$(c_{Hu})_{22}$
$\left(c_{Hq}^{(1)}\right)_{22}$	±0.679	±5.86	1			$\left(c_{Hq}^{(1)}\right)_{22}$	±0.224	±1.97	1		
$\left(c_{Hq}^{(3)}\right)_{22}$	±0.310	±0.349	−0.142	1		$\left(c_{Hq}^{(3)}\right)_{22}$	±0.117	±0.138	−0.765	1	
$(c_{Hu})_{22}$	±1.61	±13.8	0.907	−0.323	1	$(c_{Hu})_{22}$	±0.526	±4.61	0.701	−0.747	1

Table 6. Same as Table 4 but for $\left(c_{Hl}^{(1)}\right)_{33}$, $\left(c_{Hl}^{(3)}\right)_{33}$, and $(c_{He})_{33}$ from the measurements of $\mu^-\mu^+ \to \tau^-\tau^+\nu_\mu\bar{\nu}_\mu$ and $\mu^-\mu^+ \to \tau\nu_\tau\nu_\mu\mu$.

	10 TeV						30 TeV					
	68%CL 1σ bound ($\times10^{-2}$)		Correlation matrix				68%CL 1σ bound ($\times10^{-2}$)		Correlation matrix			
	Individual	Global	$\left(c_{Hl}^{(1)}\right)_{33}$	$\left(c_{Hl}^{(3)}\right)_{33}$	$(c_{He})_{33}$		Individual	Global	$\left(c_{Hl}^{(1)}\right)_{33}$	$\left(c_{Hl}^{(3)}\right)_{33}$	$(c_{He})_{33}$
$\left(c_{Hl}^{(1)}\right)_{33}$	±1.10	±8.12	1			$\left(c_{Hl}^{(1)}\right)_{33}$	±0.350	±2.72	1		
$\left(c_{Hl}^{(3)}\right)_{33}$	±0.323	±0.338	−0.00695	1		$\left(c_{Hl}^{(3)}\right)_{33}$	±0.125	±0.134	0.0388	1	
$(c_{He})_{33}$	±1.35	±10.0	0.986	0.0431	1	$(c_{He})_{33}$	±0.453	±3.53	0.946	0.156	1

energy muon collider, focusing on final states involving b,c,τ fermions. A phenomenological study is performed to estimate their potential in probing the corresponding dimension-6 operators that directly modify the couplings of the fermions (b,c,τ) to the W and Z bosons. With realistic tagging efficiencies applied, we consider only signal statistical uncertainties and extract the precision reaches on the Wilson coefficients with a chi-squared analysis on the binned signal distributions. The information in the invariant mass of the two-fermion pair turned out to be crucial for discriminating the effects of different operators and simultaneously constraining their coefficients in a global fit. The symmetric (WW fusion) and asymmetric ($WZ/W\gamma$ fusion) processes also contain complementary information. Combining all measurements, the precision of the relevant Wilson coefficients (setting $\Lambda = 1$ TeV) from a simultaneous fit with all the relevant operators in consideration (*i.e.,* those listed in Eqs. (2) and (3)) at a future muon collider can reach up to the 10^{-2} level for the 10 TeV run and up to $\sim 5\times10^{-3}$ for the 30 TeV run. For the latter, the results can be competitive with those from a future e^+e^- collider with a dedicated Z-pole run, such as the CEPC.

Our analysis demonstrates the significant potential of a future high energy muon collider in precision EW measurements, which calls for further studies in this direction. Ultimately, a complete analysis that includes all the relevant EW measurements and operators is required to fully determine the potential of a muon collider in probing EW precision physics. Our study serves as one of the many early steps towards this goal. Several directions can be taken for future studies. Most importantly, when a more concrete detector design is available, realistic analyses that include detector simulation and careful treatments of background effects and signal selection efficiencies will be required. Given the overall good statistical precision, it is also important to study the effects of systematics and theory uncertainties. These effects could be different from those of EW measurements at future e^+e^- colliders owing to the different processes and collider environments and may require dedicated studies. The usefulness of differential distributions illustrated in our study is also a call for a more sophisticated analysis of the distribution, which perhaps utilizes optimal observables [75] and/or machine learning technics (see *e.g.*, Ref. [76]). The study of the muon collider's EW physics potential is particularly relevant for the particle physics roadmap. If a muon collider is eventually built while an e^+e^- collider is not, would we miss any important physics without a Z-pole program? If both colliders are built, what important complementarity could the muon collider offer in EW precision physics? These important questions must be addressed when we make plans for future colliders.

ACKNOWLEDGMENTS

We thank Ilaria Brivio for the prompt and helpful reply to our questions regarding the SMEFTsim package. We also thank Wantong Jiang for collaborations in the early stages of this work.

Appendix A. Numerical expressions of cross section

In Tables A1−A6, contributions of relative Wilson coefficients to the cross section are formulated under different invariant mass bins and angle divisions of $|\cos\bar{\theta}|$, where only linear contributions are considered, as men-

tioned in Section II.B. The total cross sections corresponding to asymmetric processes without binning of invariant mass and angle divisions are also listed, when applicable. In all cases, Λ is set to 1 TeV.

Appendix B. Additional results

In this appendix, we illustrate the contours for other different fermion production processes mentioned in Sections IV A, IV B, and IV C.

Table A1. SM cross section and normalized SMEFT cross section ($\sigma_{\rm SMEFT}/\sigma_{\rm SM}$, as a function of Wilson coefficients) of $\mu^-\mu^+ \to b\bar{b}\nu_\mu\bar{\nu}_\mu$ for different invariant masses and $|\cos\bar{\theta}|$ bins at $\sqrt{s} = 10$ TeV. The first row corresponds to the unbinned total cross section. Tagging efficiencies are not applied here.

Invariant mass/GeV	Polar angle $\lvert\cos\bar{\theta}\rvert$	SM cross section/pb	Normalized SMEFT cross section
$[0,+\infty)$	–	0.302	$1+0.144\left(c_{Hq}^{(1)}\right)_{33}+0.131\left(c_{Hq}^{(3)}\right)_{33}-0.0226(c_{Hd})_{33}$
$[0,100)$	–	0.275	$1+0.138\left(c_{Hq}^{(1)}\right)_{33}+0.138\left(c_{Hq}^{(3)}\right)_{33}-0.0238(c_{Hd})_{33}$
$[100,200)$	–	0.0185	$1+0.137\left(c_{Hq}^{(1)}\right)_{33}+0.127\left(c_{Hq}^{(3)}\right)_{33}-0.0140(c_{Hd})_{33}$
$[200,400)$	–	0.00405	$1+0.186\left(c_{Hq}^{(1)}\right)_{33}+0.0611\left(c_{Hq}^{(3)}\right)_{33}-0.00527(c_{Hd})_{33}$
$[400,600)$	–	0.00182	$1+0.290\left(c_{Hq}^{(1)}\right)_{33}-0.0442\left(c_{Hq}^{(3)}\right)_{33}-0.00539(c_{Hd})_{33}$
$[600,800)$	≤ 0.45	1.98×10^{-4}	$1+0.622\left(c_{Hq}^{(1)}\right)_{33}-0.267\left(c_{Hq}^{(3)}\right)_{33}-0.00682(c_{Hd})_{33}$
	> 0.45	4.35×10^{-4}	$1+0.307\left(c_{Hq}^{(1)}\right)_{33}-0.111\left(c_{Hq}^{(3)}\right)_{33}-0.00631(c_{Hd})_{33}$
$[800,1000)$	≤ 0.55	1.42×10^{-4}	$1+0.810\left(c_{Hq}^{(1)}\right)_{33}-0.498\left(c_{Hq}^{(3)}\right)_{33}-0.00861(c_{Hd})_{33}$
	> 0.55	2.25×10^{-4}	$1+0.346\left(c_{Hq}^{(1)}\right)_{33}-0.152\left(c_{Hq}^{(3)}\right)_{33}-0.00749(c_{Hd})_{33}$
$[1000,1500)$	≤ 0.6	1.67×10^{-4}	$1+1.15\left(c_{Hq}^{(1)}\right)_{33}-0.879\left(c_{Hq}^{(3)}\right)_{33}-0.0116(c_{Hd})_{33}$
	> 0.6	2.61×10^{-4}	$1+0.451\left(c_{Hq}^{(1)}\right)_{33}-0.229\left(c_{Hq}^{(3)}\right)_{33}-0.00958(c_{Hd})_{33}$
$[1500,2000)$	≤ 0.65	6.17×10^{-5}	$1+1.78\left(c_{Hq}^{(1)}\right)_{33}-1.52\left(c_{Hq}^{(3)}\right)_{33}-0.0171(c_{Hd})_{33}$
	> 0.65	1.02×10^{-4}	$1+0.584\left(c_{Hq}^{(1)}\right)_{33}-0.347\left(c_{Hq}^{(3)}\right)_{33}-0.0131(c_{Hd})_{33}$
$[2000,+\infty)$	≤ 0.7	6.22×10^{-5}	$1+2.45\left(c_{Hq}^{(1)}\right)_{33}-2.09\left(c_{Hq}^{(3)}\right)_{33}-0.0279(c_{Hd})_{33}$
	> 0.7	1.17×10^{-4}	$1+0.706\left(c_{Hq}^{(1)}\right)_{33}-0.519\left(c_{Hq}^{(3)}\right)_{33}-0.0181(c_{Hd})_{33}$

Table A2. Same as Table A1 but for $\sqrt{s} = 30$ TeV.

Invariant mass/GeV	Polar angle $\lvert\cos\bar{\theta}\rvert$	SM cross section/pb	Normalized SMEFT cross section
$[0,+\infty)$	–	0.336	$1+0.147\left(c_{Hq}^{(1)}\right)_{33}+0.130\left(c_{Hq}^{(3)}\right)_{33}-0.0226(c_{Hd})_{33}$
$[0,100)$	–	0.306	$1+0.138\left(c_{Hq}^{(1)}\right)_{33}+0.138\left(c_{Hq}^{(3)}\right)_{33}-0.0237(c_{Hd})_{33}$
$[100,200)$	–	0.0207	$1+0.138\left(c_{Hq}^{(1)}\right)_{33}+0.127\left(c_{Hq}^{(3)}\right)_{33}-0.0141(c_{Hd})_{33}$
$[200,400)$	–	0.00427	$1+0.191\left(c_{Hq}^{(1)}\right)_{33}+0.0665\left(c_{Hq}^{(3)}\right)_{33}-0.00614(c_{Hd})_{33}$
$[400,600)$	–	0.00208	$1+0.258\left(c_{Hq}^{(1)}\right)_{33}-0.0462\left(c_{Hq}^{(3)}\right)_{33}-0.00607(c_{Hd})_{33}$
$[600,800)$	≤ 0.5	2.98×10^{-4}	$1+0.593\left(c_{Hq}^{(1)}\right)_{33}-0.257\left(c_{Hq}^{(3)}\right)_{33}-0.00792(c_{Hd})_{33}$
	> 0.5	4.52×10^{-4}	$1+0.297\left(c_{Hq}^{(1)}\right)_{33}-0.112\left(c_{Hq}^{(3)}\right)_{33}-0.00706(c_{Hd})_{33}$
$[800,1000)$	≤ 0.5	1.62×10^{-4}	$1+0.870\left(c_{Hq}^{(1)}\right)_{33}-0.555\left(c_{Hq}^{(3)}\right)_{33}-0.0103(c_{Hd})_{33}$
	> 0.5	2.91×10^{-4}	$1+0.383\left(c_{Hq}^{(1)}\right)_{33}-0.175\left(c_{Hq}^{(3)}\right)_{33}-0.00886(c_{Hd})_{33}$
$[1000,1500)$	≤ 0.5	1.72×10^{-4}	$1+1.45\left(c_{Hq}^{(1)}\right)_{33}-1.16\left(c_{Hq}^{(3)}\right)_{33}-0.0157(c_{Hd})_{33}$
	> 0.5	3.89×10^{-4}	$1+0.523\left(c_{Hq}^{(1)}\right)_{33}-0.294\left(c_{Hq}^{(3)}\right)_{33}-0.0121(c_{Hd})_{33}$
$[1500,2000)$	≤ 0.6	9.21×10^{-5}	$1+2.14\left(c_{Hq}^{(1)}\right)_{33}-1.86\left(c_{Hq}^{(3)}\right)_{33}-0.0248(c_{Hd})_{33}$
	> 0.6	1.46×10^{-4}	$1+0.693\left(c_{Hq}^{(1)}\right)_{33}-0.460\left(c_{Hq}^{(3)}\right)_{33}-0.0178(c_{Hd})_{33}$
$[2000,+\infty)$	≤ 0.65	1.30×10^{-4}	$1+2.10\left(c_{Hq}^{(1)}\right)_{33}-1.70\left(c_{Hq}^{(3)}\right)_{33}-0.0749(c_{Hd})_{33}$
	$> 0.$	2.21×10^{-4}	$1+0.571\left(c_{Hq}^{(1)}\right)_{33}-0.420\left(c_{Hq}^{(3)}\right)_{33}-0.0364(c_{Hd})_{33}$

Table A3. SM cross section and normalized SMEFT cross section ($\sigma_{\rm SMEFT}/\sigma_{\rm SM}$, as a function of Wilson coefficients) of $\mu^-\mu^+ \to c\bar{c}\nu_\mu\bar{\nu}_\mu$ for different invariant masses and $|\cos\bar{\theta}|$ bins at $\sqrt{s} = 10$ TeV. The first (last) row corresponds to the unbinned total cross section for $\mu^-\mu^+ \to c\bar{c}\nu_\mu\bar{\nu}_\mu$ ($\mu^-\mu^+ \to cs\nu_\mu\mu$). Tagging efficiencies are not applied here.

Invariant mass/GeV	Polar angle $\lvert\cos\bar{\theta}\rvert$	SM cross section/pb	Normalized SMEFT cross section
$[0,+\infty)$	–	0.216	$1-0.142\left(c_{Hq}^{(1)}\right)_{22}+0.148\left(c_{Hq}^{(3)}\right)_{22}+0.0604\,(c_{Hu})_{22}$
$[0,100)$	–	0.199	$1-0.144\left(c_{Hq}^{(1)}\right)_{22}+0.146\left(c_{Hq}^{(3)}\right)_{22}+0.0622\,(c_{Hu})_{22}$
$[100,200)$	–	0.01395	$1-0.140\left(c_{Hq}^{(1)}\right)_{22}+0.139\left(c_{Hq}^{(3)}\right)_{22}+0.0363\,(c_{Hu})_{22}$
$[200,400)$	–	0.00252	$1-0.0823\left(c_{Hq}^{(1)}\right)_{22}+0.164\left(c_{Hq}^{(3)}\right)_{22}+0.0176\,(c_{Hu})_{22}$
$[400,600)$	–	8.29×10^{-4}	$1-0.0294\left(c_{Hq}^{(1)}\right)_{22}+0.210\left(c_{Hq}^{(3)}\right)_{22}+0.0247\,(c_{Hu})_{22}$
$[600,800)$	≤ 0.45	1.04×10^{-4}	$1+0.0376\left(c_{Hq}^{(1)}\right)_{22}+0.373\left(c_{Hq}^{(3)}\right)_{22}+0.0488\,(c_{Hu})_{22}$
	> 0.45	2.86×10^{-4}	$1+0.0141\left(c_{Hq}^{(1)}\right)_{22}+0.218\left(c_{Hq}^{(3)}\right)_{22}+0.0292\,(c_{Hu})_{22}$
$[800,1000)$	≤ 0.45	5.38×10^{-5}	$1+0.152\left(c_{Hq}^{(1)}\right)_{22}+0.496\left(c_{Hq}^{(3)}\right)_{22}+0.0684\,(c_{Hu})_{22}$
	> 0.45	1.58×10^{-4}	$1+0.0513\left(c_{Hq}^{(1)}\right)_{22}+0.252\left(c_{Hq}^{(3)}\right)_{22}+0.0368\,(c_{Hu})_{22}$
$[1000,1500)$	≤ 0.45	5.79×10^{-5}	$1+0.402\left(c_{Hq}^{(1)}\right)_{22}+0.750\left(c_{Hq}^{(3)}\right)_{22}+0.104\,(c_{Hu})_{22}$
	> 0.45	1.72×10^{-4}	$1+0.129\left(c_{Hq}^{(1)}\right)_{22}+0.330\left(c_{Hq}^{(3)}\right)_{22}+0.0493\,(c_{Hu})_{22}$
$[1500,2000)$	≤ 0.5	2.51×10^{-5}	$1+0.956\left(c_{Hq}^{(1)}\right)_{22}+1.29\left(c_{Hq}^{(3)}\right)_{22}+0.158\,(c_{Hu})_{22}$
	> 0.5	5.48×10^{-5}	$1+0.305\left(c_{Hq}^{(1)}\right)_{22}+0.495\left(c_{Hq}^{(3)}\right)_{22}+0.0699\,(c_{Hu})_{22}$
$[2000,+\infty)$	≤ 0.6	3.63×10^{-5}	$1+3.36\left(c_{Hq}^{(1)}\right)_{22}+3.66\left(c_{Hq}^{(3)}\right)_{22}+0.234\,(c_{Hu})_{22}$
	> 0.6	4.27×10^{-5}	$1+0.980\left(c_{Hq}^{(1)}\right)_{22}+1.14\left(c_{Hq}^{(3)}\right)_{22}+0.0992\,(c_{Hu})_{22}$
$\mu^-\mu^+ \to cs\nu_\mu\mu$	–	0.0144	$1-1.92\times10^{-4}\left(c_{Hq}^{(1)}\right)_{22}-0.121\left(c_{Hq}^{(3)}\right)_{22}-7.16\times10^{-11}\,(c_{Hu})_{22}$

Table A4. Same as Table A3 but for $\sqrt{s} = 30$ TeV.

Invariant mass/GeV	Polar angle $\lvert\cos\bar{\theta}\rvert$	SM cross section/pb	Normalized SMEFT cross section
$[0,+\infty)$	–	0.225	$1-0.133\left(c_{Hq}^{(1)}\right)_{22}+0.155\left(c_{Hq}^{(3)}\right)_{22}+0.0600\,(c_{Hu})_{22}$
$[0,100)$	–	0.206	$1-0.143\left(c_{Hq}^{(1)}\right)_{22}+0.146\left(c_{Hq}^{(3)}\right)_{22}+0.0622\,(c_{Hu})_{22}$
$[100,200)$	–	0.0138	$1-0.136\left(c_{Hq}^{(1)}\right)_{22}+0.137\left(c_{Hq}^{(3)}\right)_{22}+0.0367\,(c_{Hu})_{22}$
$[200,400)$	–	0.00261	$1-0.0980\left(c_{Hq}^{(1)}\right)_{22}+0.184\left(c_{Hq}^{(3)}\right)_{22}+0.0174\,(c_{Hu})_{22}$
$[400,600)$	–	0.00105	$1-0.0371\left(c_{Hq}^{(1)}\right)_{22}+0.204\left(c_{Hq}^{(3)}\right)_{22}+0.0249\,(c_{Hu})_{22}$
$[600,800)$	≤ 0.45	1.44×10^{-4}	$1+0.0138\left(c_{Hq}^{(1)}\right)_{22}+0.357\left(c_{Hq}^{(3)}\right)_{22}+0.0471\,(c_{Hu})_{22}$
	> 0.45	3.95×10^{-4}	$1+0.00529\left(c_{Hq}^{(1)}\right)_{22}+0.210\left(c_{Hq}^{(3)}\right)_{22}+0.0284\,(c_{Hu})_{22}$
$[800,1000)$	≤ 0.45	7.85×10^{-5}	$1+0.115\left(c_{Hq}^{(1)}\right)_{22}+0.489\left(c_{Hq}^{(3)}\right)_{22}+0.0678\,(c_{Hu})_{22}$
	> 0.45	2.42×10^{-4}	$1+0.0393\left(c_{Hq}^{(1)}\right)_{22}+0.236\left(c_{Hq}^{(3)}\right)_{22}+0.0347\,(c_{Hu})_{22}$
$[1000,1500)$	≤ 0.5	1.20×10^{-4}	$1+0.320\left(c_{Hq}^{(1)}\right)_{22}+0.679\left(c_{Hq}^{(3)}\right)_{22}+0.0959\,(c_{Hu})_{22}$
	> 0.5	2.81×10^{-4}	$1+0.103\left(c_{Hq}^{(1)}\right)_{22}+0.298\left(c_{Hq}^{(3)}\right)_{22}+0.0442\,(c_{Hu})_{22}$
$[1500,2000)$	≤ 0.5	5.08×10^{-5}	$1+0.919\left(c_{Hq}^{(1)}\right)_{22}+1.27\left(c_{Hq}^{(3)}\right)_{22}+0.159\,(c_{Hu})_{22}$
	> 0.5	1.22×10^{-4}	$1+0.252\left(c_{Hq}^{(1)}\right)_{22}+0.441\left(c_{Hq}^{(3)}\right)_{22}+0.0637\,(c_{Hu})_{22}$
$[2000,+\infty)$	≤ 0.6	1.22×10^{-4}	$1+12.1\left(c_{Hq}^{(1)}\right)_{22}+12.3\left(c_{Hq}^{(3)}\right)_{22}+0.336\,(c_{Hu})_{22}$
	> 0.6	1.50×10^{-4}	$1+2.79\left(c_{Hq}^{(1)}\right)_{22}+3.02\left(c_{Hq}^{(3)}\right)_{22}+0.113\,(c_{Hu})_{22}$
$\mu^-\mu^+ \to cs\nu_\mu\mu$	–	0.520	$1-3.22\times10^{-6}\left(c_{Hq}^{(1)}\right)_{22}+0.126\left(c_{Hq}^{(3)}\right)_{22}-4.19\times10^{-8}\,(c_{Hu})_{22}$

Table A5. SM cross section and normalized SMEFT cross section ($\sigma_{\rm SMEFT}/\sigma_{\rm SM}$, as a function of Wilson coefficients) of $\mu^-\mu^+ \to \tau^-\tau^+\nu_\mu\bar{\nu}_\mu$ for different invariant mass and $\cos\bar{\theta}$ bins at $\sqrt{s} = 10$ TeV. The first (last) row corresponds to the unbinned total cross section for $\mu^-\mu^+ \to \tau^-\tau^+\nu_\mu\bar{\nu}_\mu$ ($\mu^-\mu^+ \to \tau\nu\bar{\tau}\nu_\mu\mu$). Tagging efficiencies are not applied here.

Invariant mass/GeV	Polar angle $\cos\bar{\theta}$	SM cross section/pb	Normalized SMEFT cross section
$[0,+\infty)$	–	0.0740	$1+0.127\left(c_{Hl}^{(1)}\right)_{33}+0.132\left(c_{Hl}^{(3)}\right)_{33}-0.102(c_{He})_{33}$
$[0,100)$	–	0.0689	$1+0.126\left(c_{Hl}^{(1)}\right)_{33}+0.127\left(c_{Hl}^{(3)}\right)_{33}-0.105(c_{He})_{33}$
$[100,200)$	–	0.00452	$1+0.138\left(c_{Hl}^{(1)}\right)_{33}+0.143\left(c_{Hl}^{(3)}\right)_{33}-0.0615(c_{He})_{33}$
$[200,400)$	–	9.24×10^{-4}	$1+0.0776\left(c_{Hl}^{(1)}\right)_{33}+0.167\left(c_{Hl}^{(3)}\right)_{33}-0.0241(c_{He})_{33}$
$[400,600)$	–	3.35×10^{-4}	$1+0.0338\left(c_{Hl}^{(1)}\right)_{33}+0.205\left(c_{Hl}^{(3)}\right)_{33}-0.0304(c_{He})_{33}$
$[600,800)$	≤ 0.5	5.34×10^{-5}	$1+0.00797\left(c_{Hl}^{(1)}\right)_{33}+0.299\left(c_{Hl}^{(3)}\right)_{33}-0.0536(c_{He})_{33}$
	>0.5	1.19×10^{-4}	$1+0.00456\left(c_{Hl}^{(1)}\right)_{33}+0.200\left(c_{Hl}^{(3)}\right)_{33}-0.0320(c_{He})_{33}$
$[800,1000)$	≤ 0.5	2.83×10^{-5}	$1-0.0291\left(c_{Hl}^{(1)}\right)_{33}+0.358\left(c_{Hl}^{(3)}\right)_{33}-0.0726(c_{He})_{33}$
	>0.5	7.42×10^{-5}	$1-0.0141\left(c_{Hl}^{(1)}\right)_{33}+0.213\left(c_{Hl}^{(3)}\right)_{33}-0.0362(c_{He})_{33}$
$[1000,1500)$	≤ 0.6	4.84×10^{-5}	$1-0.0712\left(c_{Hl}^{(1)}\right)_{33}+0.376\left(c_{Hl}^{(3)}\right)_{33}-0.0823(c_{He})_{33}$
	>0.6	7.97×10^{-5}	$1-0.0329\left(c_{Hl}^{(1)}\right)_{33}+0.227\left(c_{Hl}^{(3)}\right)_{33}-0.0408(c_{He})_{33}$
$[1500,2000)$	≤ 0.7	2.49×10^{-5}	$1-0.131\left(c_{Hl}^{(1)}\right)_{33}+0.441\left(c_{Hl}^{(3)}\right)_{33}-0.103(c_{He})_{33}$
	>0.7	3.04×10^{-5}	$1-0.0524\left(c_{Hl}^{(1)}\right)_{33}+0.231\left(c_{Hl}^{(3)}\right)_{33}-0.0453(c_{He})_{33}$
$[2000,+\infty)$	≤ 0.75	3.30×10^{-5}	$1-0.200\left(c_{Hl}^{(1)}\right)_{33}+0.539\left(c_{Hl}^{(3)}\right)_{33}-0.128(c_{He})_{33}$
	>0.75	4.38×10^{-5}	$1-0.0679\left(c_{Hl}^{(1)}\right)_{33}+0.224\left(c_{Hl}^{(3)}\right)_{33}-0.0492(c_{He})_{33}$
$\mu^-\mu^+ \to \tau\nu\bar{\tau}\nu_\mu\mu$	–	0.351	$1-6.83\times10^{-5}\left(c_{Hl}^{(1)}\right)_{33}+0.122\left(c_{Hl}^{(3)}\right)_{33}-5.55\times10^{-8}(c_{He})_{33}$

Table A6. Same as Table A5 but for $\sqrt{s} = 30$ TeV.

Invariant mass/GeV	Polar angle $\lvert\cos\bar{\theta}\rvert$	SM cross section/pb	Normalized SMEFT cross section
$[0,+\infty)$	–	0.0800	$1+0.126\left(c_{Hl}^{(1)}\right)_{33}+0.131\left(c_{Hl}^{(3)}\right)_{33}-0.102(c_{He})_{33}$
$[0,100)$	–	0.0721	$1+0.129\left(c_{Hl}^{(1)}\right)_{33}+0.130\left(c_{Hl}^{(3)}\right)_{33}-0.102(c_{He})_{33}$
$[100,200)$	–	0.00464	$1+0.141\left(c_{Hl}^{(1)}\right)_{33}+0.145\left(c_{Hl}^{(3)}\right)_{33}-0.0626(c_{He})_{33}$
$[200,400)$	–	0.00102	$1+0.0792\left(c_{Hl}^{(1)}\right)_{33}+0.166\left(c_{Hl}^{(3)}\right)_{33}-0.0267(c_{He})_{33}$
$[400,600)$	–	3.73×10^{-4}	$1+0.0346\left(c_{Hl}^{(1)}\right)_{33}+0.207\left(c_{Hl}^{(3)}\right)_{33}-0.0349(c_{He})_{33}$
$[600,800)$	≤ 0.5	6.73×10^{-5}	$1+0.000268\left(c_{Hl}^{(1)}\right)_{33}+0.300\left(c_{Hl}^{(3)}\right)_{33}-0.0617(c_{He})_{33}$
	>0.5	1.32×10^{-4}	$1+0.000162\left(c_{Hl}^{(1)}\right)_{33}+0.203\left(c_{Hl}^{(3)}\right)_{33}-0.0365(c_{He})_{33}$
$[800,1000)$	≤ 0.5	3.71×10^{-5}	$1-0.0469\left(c_{Hl}^{(1)}\right)_{33}+0.372\left(c_{Hl}^{(3)}\right)_{33}-0.0864(c_{He})_{33}$
	>0.5	8.31×10^{-5}	$1-0.0245\left(c_{Hl}^{(1)}\right)_{33}+0.222\left(c_{Hl}^{(3)}\right)_{33}-0.0435(c_{He})_{33}$
$[1000,1500)$	≤ 0.55	5.56×10^{-5}	$1-0.124\left(c_{Hl}^{(1)}\right)_{33}+0.448\left(c_{Hl}^{(3)}\right)_{33}-0.116(c_{He})_{33}$
	>0.55	1.01×10^{-4}	$1-0.0564\left(c_{Hl}^{(1)}\right)_{33}+0.251\left(c_{Hl}^{(3)}\right)_{33}-0.0539(c_{He})_{33}$
$[1500,2000)$	≤ 0.5	1.85×10^{-5}	$1-0.301\left(c_{Hl}^{(1)}\right)_{33}+0.702\left(c_{Hl}^{(3)}\right)_{33}-0.222(c_{He})_{33}$
	>0.5	5.32×10^{-5}	$1-0.116\left(c_{Hl}^{(1)}\right)_{33}+0.300\left(c_{Hl}^{(3)}\right)_{33}-0.0723(c_{He})_{33}$
$[2000,+\infty)$	≤ 0.6	4.35×10^{-5}	$1-0.727\left(c_{Hl}^{(1)}\right)_{33}+1.09\left(c_{Hl}^{(3)}\right)_{33}-0.444(c_{He})_{33}$
	>0.6	8.61×10^{-5}	$1-0.283\left(c_{Hl}^{(1)}\right)_{33}+0.457\left(c_{Hl}^{(3)}\right)_{33}-0.113(c_{He})_{33}$
$\mu^-\mu^+ \to \tau\nu_\tau\nu_\mu\mu$	–	0.248	$1-9.16\times10^{-5}\left(c_{Hl}^{(1)}\right)_{33}+0.121\left(c_{Hl}^{(3)}\right)_{33}-8.98\times10^{-8}(c_{He})_{33}$

Fig. B1 and Fig. B2 show the $\Delta\chi^2 = 1$ contours with invariant mass bins, similar to Fig. 7, but for $\mu^-\mu^+ \to c\bar{c}\nu_\mu\bar{\nu}_\mu$ and $\mu^-\mu^+ \to \tau^-\tau^+\nu_\mu\bar{\nu}_\mu$, respectively. Fig. B3 and Fig. B4 show the comparisons of the results with and without including the $|\cos\bar{\theta}|$ bins, similar to Fig. 8, but for $\mu^-\mu^+ \to c\bar{c}\nu_\mu\bar{\nu}_\mu$ and $\mu^-\mu^+ \to \tau^-\tau^+\nu_\mu\bar{\nu}_\mu$, respectively. Fig. B5 shows the comparison of asymmetric processes with and without inclusion, similar to Fig. 9, but for the processes $\mu^-\mu^+ \to c\bar{c}\nu_\mu\bar{\nu}_\mu$ and $\mu^-\mu^+ \to cs\nu_\mu\mu$.

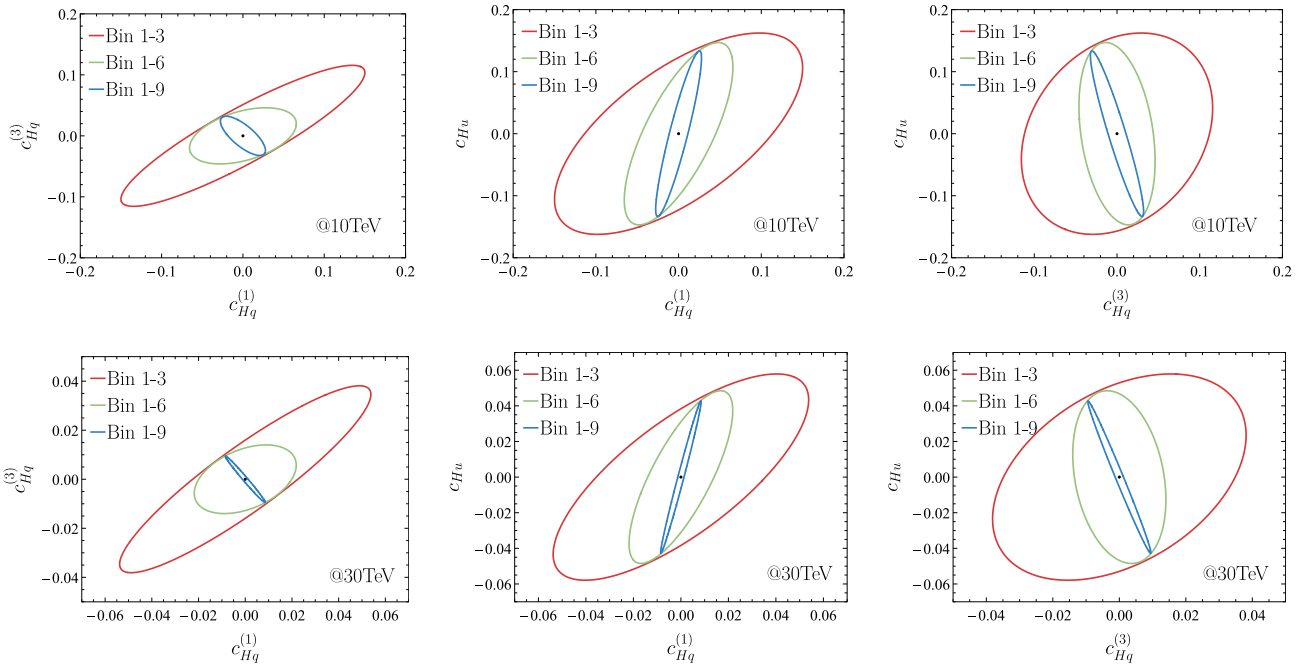

Fig. B1. (color online) Similar to Fig. 7, the $\Delta\chi^2 = 1$ contours from the three-parameter $(c_{Hq}^{(1)}, c_{Hq}^{(3)}, c_{Hu})$ are shown for $\mu^-\mu^+ \to c\bar{c}\nu_\mu\bar{\nu}_\mu$ at 10 TeV (top row) and 30 TeV (bottom row), with the invariant mass bins from Table 2. For each row, the results are projected onto three 2D planes (each with the other parameter marginalized). Only the contours with the first three, six, and all nine bins are shown.

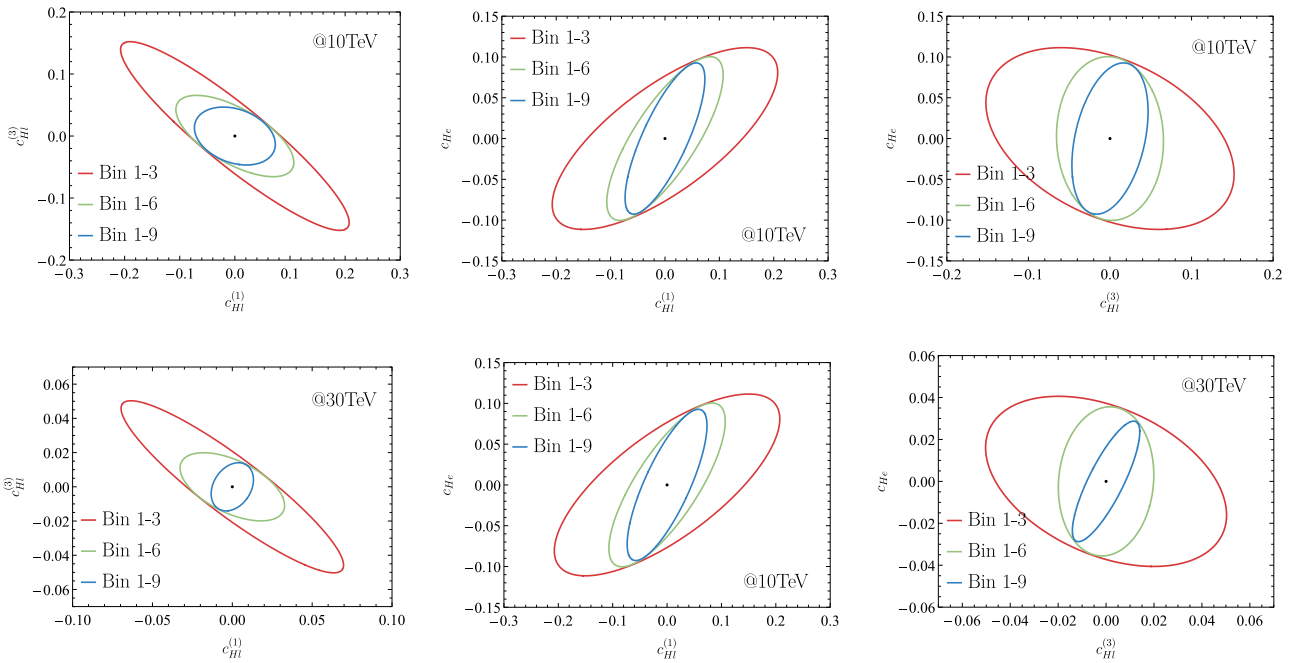

Fig. B2. (color online) Similar to Fig. B1 but for $\mu^-\mu^+ \to \tau^-\tau^+\nu_\mu\bar{\nu}_\mu$ with Wilson coefficients $c_{Hl}^{(1)}$, $c_{Hl}^{(3)}$, and c_{He}.

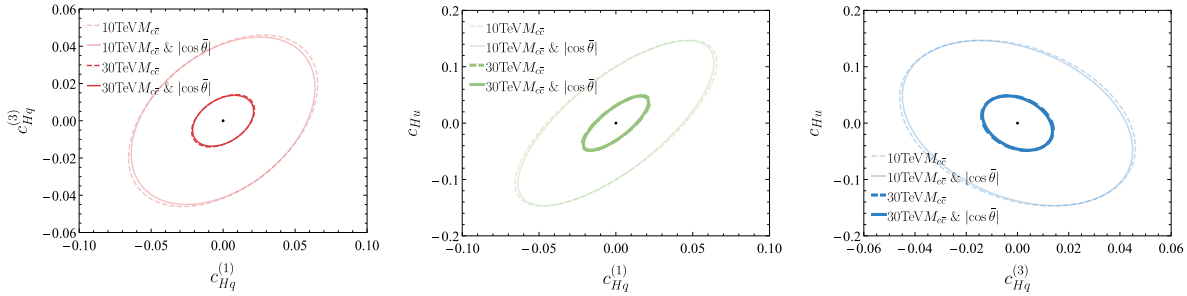

Fig. B3. (color online) Similar to Fig. 8, the comparison of the results is shown for $\mu^-\mu^+ \to c\bar{c}\nu_\mu\bar{\nu}_\mu$ with only the invariant mass bins (dashed contours, binning as in Table 2) and with the $|\cos\bar{\theta}|$ bins (solid contours, binning as in Table 3). An invariant mass cut of $M_{c\bar{c}} < 1$ TeV is imposed. The contours correspond to $\Delta\chi^2 = 1$ from the 3-parameter $(c_{Hq}^{(1)}, c_{Hq}^{(3)}, c_{Hu})$ fit.

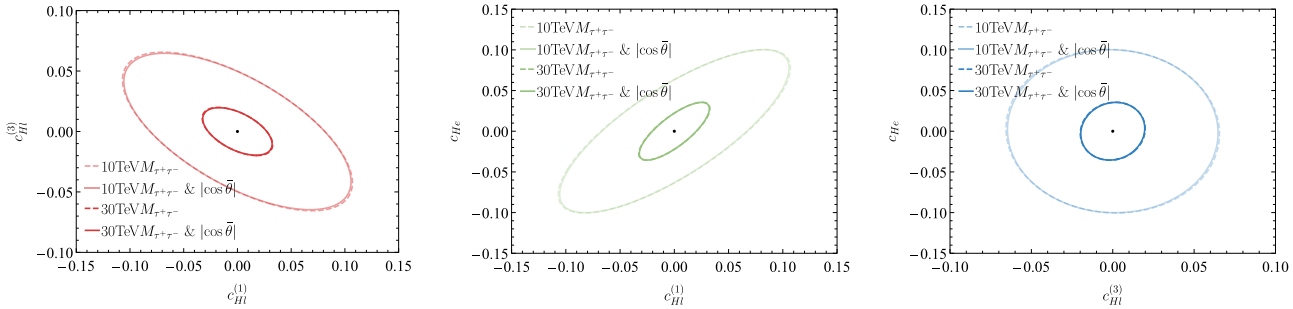

Fig. B4. (color online) Similar to Fig. B3 but for $\mu^-\mu^+ \to \tau^-\tau^+\nu_\mu\bar{\nu}_\mu$ with Wilson coefficients $c_{Hl}^{(1)}$, $c_{Hl}^{(3)}$, and c_{He}.

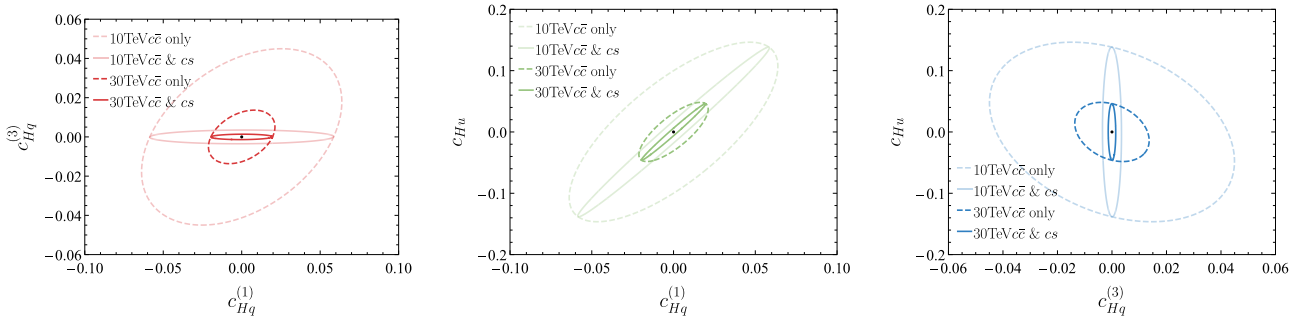

Fig. B5. (color online) Similar to Fig. 9; comparison of the results for the three parameters $c_{Hq}^{(1)}, c_{Hq}^{(3)}, c_{Hu}$ from the measurements of $\mu^-\mu^+ \to c\bar{c}\nu_\mu\bar{\nu}_\mu$ only (labeled as "$c\bar{c}$ only", dashed contours, with $M_{c\bar{c}} < 1$ TeV) and the combination of $\mu^-\mu^+ \to c\bar{c}\nu_\mu\bar{\nu}_\mu$ and $\mu^-\mu^+ \to cs\nu_\mu\mu$ (labeled as "$c\bar{c}$&cs", solid contours). Contours corresponds to $\Delta\chi^2 = 1$.

References

[1] H. Al Ali *et al.*, Rept. Prog. Phys. **85**, 084201 (2022)
[2] C. Aime *et al.*, (2022), arXiv: 2203.07256
[3] C. Accettura *et al.*, Eur. Phys. J. C **83**, 864 (2023) [Erratum: Eur. Phys. J. C **84**, 36 (2024)]
[4] M. Narain *et al.*, (2022), arXiv: 2211.11084
[5] European Strategy Group, *2020 Update of the European Strategy for Particle Physics* (CERN Council, Geneva, 2020)
[6] International muon collider collaboration, (2025), 2025-03-02. https://muoncollider.web.cern.ch/
[7] C. Accettura *et al.* (International Muon Collider), **2/2024** (2024), 10.23731/CYRM-2024-002, arXiv: 2407.12450
[8] C. Adolphsen *et al.*, CERN Yellow Rep. Monogr. **1**, 1 (2022)
[9] M. Dong *et al.* (CEPC Study Group), (2018), arXiv: 1811.10545
[10] H. Cheng *et al.* (CEPC Physics Study Group), in *Snowmass 2021*, (2022), arXiv: 2205.08553
[11] A. Abada *et al.*, Eur. Phys. J. ST **228**, 261 (2019)
[12] G. Bernardi *et al.*, (2022), arXiv: 2203.06520
[13] A. Aryshev *et al.* (ILC International Development Team), (2022), arXiv: 203.07622
[14] M. Bai *et al.*, in *Snowmass 2021*, (2021), arXiv: 2110.15800
[15] T. K. Charles *et al.* (CLICdp, CLIC), **2/2018** (2018), 10.23731/CYRM-2018-002, arXiv: 1812.06018
[16] J. de Blas *et al.* (CLIC), **3/2018** (2018), 10.23731/CYRM-

2018-003, arXiv: 1812.02093
[17] J. de Blas *et al.* (Muon Collider), (2022), arXiv: 2203.07261
[18] V. D. Barger, M. S. Berger, J. F. Gunion *et al.*, Phys. Rev. Lett. **75**, 1462 (1995)
[19] V. D. Barger, M. S. Berger, J. F. Gunion *et al.*, Phys. Rept. **286**, 1 (1997)
[20] J. de Blas, J. Gu, and Z. Liu, Phys. Rev. D **106**, 073007 (2022)
[21] R. Franceschini, G. Panico, A. Pomarol *et al.*, JHEP **02**, 111 (2018)
[22] D. Buttazzo, R. Franceschini, and A. Wulzer, JHEP **05**, 219 (2021)
[23] T. Han, Y. Ma, and K. Xie, Phys. Rev. D **103**, L031301 (2021)
[24] T. Han, D. Liu, I. Low *et al.*, Phys. Rev. D **103**, 013002 (2021)
[25] A. Costantini, F. De Lillo, F. Maltoni *et al.*, JHEP **09**, 080 (2020)
[26] M. Forslund and P. Meade, JHEP **08**, 185 (2022)
[27] T. Han, D. Liu, I. Low *et al.*, Phys. Rev. D **110**, 013005 (2024)
[28] W. Buchmuller and D. Wyler, Nucl. Phys. B **268**, 621 (1986)
[29] B. Grzadkowski, M. Iskrzynski, M. Misiak *et al.*, JHEP **10**, 085 (2010)
[30] A. Falkowski, M. Gonzalez-Alonso, A. Greljo *et al.*, Phys. Rev. Lett. **116**, 011801 (2016)
[31] G. Durieux, C. Grojean, J. Gu *et al.*, JHEP **09**, 014 (2017)
[32] T. Barklow, K. Fujii, S. Jung, *et al.*, Phys. Rev. D **97**, 053003 (2018)
[33] G. Durieux, M. Perelló, M. Vos *et al.*, JHEP **10**, 168 (2018)
[34] G. Durieux, J. Gu, E. Vryonidou *et al.*, Chin. Phys. C **42**, 123107 (2018)
[35] J. Ellis, C. W. Murphy, V. Sanz *et al.*, JHEP **06**, 146 (2018)
[36] J. De Blas, G. Durieux, C. Grojean *et al.*, JHEP **12**, 117 (2019)
[37] G. Durieux, A. Irles, V. Miralles *et al.*, JHEP **12**, 98 (2019) [Erratum: JHEP **01**, 195 (2021)]
[38] J. Ellis, M. Madigan, K. Mimasu *et al.*, JHEP **04**, 279 (2021)
[39] V. Miralles, M. M. López, M. M. Llácer *et al.*, JHEP **02**, 032 (2022)
[40] J. J. Ethier *et al.* (SMEFiT), JHEP **11**, 089 (2021)
[41] S. Bruggisser, D. van Dyk, and S. Westhoff, JHEP **02**, 225 (2023)
[42] Y. Liu, Y. Wang, C. Zhang *et al.*, Chin. Phys. C **46**, 113105 (2022)
[43] J. de Blas, Y. Du, C. Grojean *et al.*, in *Snowmass 2021*, (2022), arXiv: 2206.08326
[44] I. Brivio, S. Bruggisser, N. Elmer *et al.*, SciPost Phys. **16**, 035 (2024)
[45] R. Aoude, F. Maltoni, O. Mattelaer *et al.*, JHEP **09**, 191 (2023)
[46] R. Bartocci, A. Biekötter, and T. Hurth, JHEP **05**, 074 (2024)
[47] L. Allwicher, C. Cornella, G. Isidori *et al.*, JHEP **03**, 049 (2024)
[48] C. Grunwald, G. Hiller, K. Kröninger *et al.*, JHEP **11**, 110 (2023)
[49] F. Garosi, D. Marzocca, A. R. Sánchez *et al.*, JHEP **12**, 129 (2023)
[50] N. Elmer, M. Madigan, T. Plehn *et al.*, (2023), arXiv: 2312.12502
[51] Z. Kassabov, M. Madigan, L. Mantani *et al.*, JHEP **05**, 205 (2023)
[52] L. Bellafronte, S. Dawson, and P. P. Giardino, JHEP **05**, 208 (2023)
[53] E. Celada, T. Giani, J. ter Hoeve *et al.*, JHEP **09**, 091 (2024)
[54] K. Asteriadis, S. Dawson, P. P. Giardino *et al.*, Phys. Rev. Lett. **133**, 231801 (2024)
[55] R. Bartocci, A. Biekötter, and T. Hurth, (2024), arXiv: 2412.09674
[56] H. El Faham, K. Mimasu, D. Pagani *et al.*, (2024), arXiv: 2412.16076
[57] H. El Faham, G. Pelliccioli, and E. Vryonidou, JHEP **08**, 087 (2024)
[58] A. Biekötter and B. D. Pecjak, (2025), arXiv: 2503.07724
[59] F. Cornet-Gomez, V. Miralles, M. Miralles López *et al.*, (2025), arXiv: 2503.11518
[60] J. ter Hoeve, L. Mantani, A. N. Rossia *et al.*, (2025), arXiv: 2502.20453
[61] V. Maura, B. A. Stefanek, and T. You, (2025), arXiv: 2503.13719
[62] J. Alwall, M. Herquet, F. Maltoni *et al.*, JHEP **06**, 128 (2011)
[63] M. Ruhdorfer, E. Salvioni, and A. Wulzer, Phys. Rev. D **107**, 095038 (2023)
[64] M. Ruhdorfer, E. Salvioni, and A. Wulzer, (2024), arXiv: 2411.00096
[65] P. Li, Z. Liu, and K. F. Lyu, Phys. Rev. D **109**, 073009 (2024)
[66] D. Buarque Franzosi *et al.*, Rev. Phys. **8**, 100071 (2022)
[67] T. Han, Y. Ma, and K. Xie, JHEP **02**, 154 (2022)
[68] J. Alwall, R. Frederix, S. Frixione *et al.*, JHEP **07**, 079 (2014)
[69] I. Brivio, JHEP **04**, 073 (2021)
[70] L. Darmé *et al.*, Eur. Phys. J. C **83**, 631 (2023)
[71] H. Liang, Y. Zhu, Y. Wang *et al.*, Phys. Rev. Lett. **132**, 221802 (2024)
[72] T. Suehara and T. Tanabe, Nucl. Instrum. Meth. A **808**, 109 (2016)
[73] R. Contino, A. Falkowski, F. Goertz *et al.*, JHEP **07**, 144 (2016)
[74] S. Alte, M. König, and W. Shepherd, JHEP **01**, 094 (2018)
[75] M. Diehl and O. Nachtmann, Z. Phys. C **62**, 397 (1994)
[76] S. Chai, J. Gu, and L. Li, JHEP **05**, 292 (2024)